



## RESEARCH ARTICLE

# Sub-voxel quantitative susceptibility mapping for assessing whole-brain magnetic susceptibility from ages 4 to 80

Guoyan Lao<sup>1</sup>  | Qiangqiang Liu<sup>2</sup> | Zhenghao Li<sup>1</sup> | Xiaojun Guan<sup>3</sup> |  
Xiaojun Xu<sup>3</sup>  | Yuyao Zhang<sup>4</sup> | Hongjiang Wei<sup>1</sup>

<sup>1</sup>School of Biomedical Engineering, Shanghai Jiao Tong University, Shanghai, China

<sup>2</sup>Department of Neurosurgery, Clinical Neuroscience Center Comprehensive Epilepsy Unit, Ruijin Hospital, Shanghai Jiao Tong University School of Medicine, Shanghai, China

<sup>3</sup>Department of Radiology, The Second Affiliated Hospital of Zhejiang University, Zhejiang University School of Medicine, Hangzhou, China

<sup>4</sup>School of Information and Science and Technology, ShanghaiTech University, Shanghai, China

## Correspondence

Hongjiang Wei, School of Biomedical Engineering, Shanghai Jiao Tong University, 1954 Huashan Rd, MED-X Research Institute, Shanghai 200030, China.  
Email: [hongjiang.wei@sjtu.edu.cn](mailto:hongjiang.wei@sjtu.edu.cn)

## Funding information

Fundamental Research Funds for the Central Universities, Grant/Award Number: ZXWH1082101; National Natural Science Foundation of China, Grant/Award Numbers: 61901256, 91949120, 62071299; Shanghai Science and Technology Development Funds, Grant/Award Number: 21DZ1100300; SJTU Trans-med Awards Research, Grant/Award Number: STAR 20220103

## Abstract

The evolution of magnetic susceptibility of the brain is mainly determined by myelin in white matter (WM) and iron deposition in deep gray matter (DGM). However, existing imaging techniques have limited abilities to simultaneously quantify the myelination and iron deposition within a voxel throughout brain development and aging. For instance, the temporal trajectories of iron in the brain WM and myelination in DGM have not been investigated during the aging process. This study aimed to map the age-related iron and myelin changes in the whole brain, encompassing myelin in DGM and iron deposition in WM, using a novel sub-voxel quantitative susceptibility mapping (QSM) method. To achieve this, a cohort of 494 healthy adults (18–80 years old) was studied. The sub-voxel QSM method was employed to obtain the paramagnetic and diamagnetic susceptibility based on the approximated  $R_2'$  map from acquired  $R_2^*$  map. The linear relationship between  $R_2^*$  and  $R_2'$  maps was established from the regression coefficients on a small cohort data acquired with both 3D gradient recalled echo data and  $R_2$  mapping. Large cohort sub-voxel susceptibility maps were used to create longitudinal and age-specific atlases via group-wise registration. To explore the differential developmental trajectories in the DGM and WM, we employed nonlinear models including exponential and Poisson functions, along with generalized additive models. The constructed atlases reveal the iron accumulation in the posterior part of the putamen and the gradual myelination process in the globus pallidus with aging. Interestingly, the developmental trajectories show that the rate of myelination differs among various DGM regions. Furthermore, the process of myelin synthesis is paralleled by an associated pattern of iron accumulation in the primary WM fiber bundles. In summary, our study offers significant insights into the distinctive developmental trajectories of iron in the brain's WM and myelination/demyelination in the DGM in vivo. These findings highlight the potential of using sub-voxel QSM to uncover new perspectives in neuroscience and improve our understanding of whole-brain myelination and iron deposit processes across the lifespan.

This is an open access article under the terms of the [Creative Commons Attribution-NonCommercial-NoDerivs](https://creativecommons.org/licenses/by-nc-nd/4.0/) License, which permits use and distribution in any medium, provided the original work is properly cited, the use is non-commercial and no modifications or adaptations are made.

© 2023 The Authors. *Human Brain Mapping* published by Wiley Periodicals LLC.

## KEYWORDS

atlas construction, brain development, iron quantification, myelin quantification, quantitative susceptibility mapping, susceptibility source separation

## 1 | INTRODUCTION

It is known that iron deposition plays a critical role in various neurological processes such as myelin synthesis and maintenance, myelin production and metabolism of neurotransmitters (Algarin et al., 2003; German & Juul, 2021). The tight association of iron deposition with axonal myelination during brain development has been reported (Ward et al., 2014). Previous studies have extensively investigated the distribution and accumulation of iron in the brain. Hallgren et al. reported a progressive accumulation of iron in the basal ganglia and the cerebral cortex by iron staining (Hallgren & Sourander, 1958). Ramos et al. demonstrated the heterogeneous iron distribution in the brain using graphite furnace atomic absorption spectrometry, with the highest level found in putamen and the lowest in the medulla (Ramos et al., 2014). Haacke et al. explored the response of iron in the brain that produces signal changes in both magnitude and phase images as revealed by MRI and suggested a correlation between these images and the iron content in the brain (Haacke et al., 2005). Quantitative susceptibility mapping (QSM) is an MRI postprocessing technique that allows for non-invasive quantification of the bulk magnetic susceptibility of brain tissue. To date, QSM has already been widely used to assess magnetic susceptibility changes of paramagnetic iron and diamagnetic myelin in the brain (Wei Li et al., 2011; Liu et al., 2015; Schweser et al., 2011). For example, previous studies have shown that iron concentration is unevenly distributed in the brain, with the basal ganglia exhibiting the highest iron content. It has also been demonstrated that myelination occurs during brain development and demyelination occurs in white matter (WM)-related diseases (Bartzokis et al., 2007; Connor, 2004). The validity of QSM as a suitable in vivo imaging technique to map the temporal trajectories of iron and myelin in normal brain development has been demonstrated in earlier studies (Betts et al., 2016; C. He et al., 2022).

Myelin is produced not only in the brain WM but also in the gray matter (GM). The Schaltenbrand and Wahren atlas (Schaltenbrand & Wahren, 1977) reveals evident myelin staining results in the globus pallidus (GP). Bao et al. (2021) also investigated a thin internal medullary lamina between external GP (GPe) and internal GP (GPi) on susceptibility tensor images. However, myelination and demyelination in GM have been relatively understudied, which might provide new views for understanding the biophysical mechanisms of various neurodegenerative diseases. Likewise, iron also plays a crucial role in WM generation, with both human and animal studies showing that iron is necessary for myelin synthesis and maintenance (Algarin et al., 2003; Ortiz et al., 2004). Iron deficiency may result in a retarded myelination during brain development, while iron overload would result in neurodegeneration and demyelination (Bartzokis et al., 2007; Connor, 2004; Roncagliolo et al., 1998; Todorich & Connor, 2004). However,

traditional QSM methods cannot differentiate molecular sources with opposing susceptibility sources, such as paramagnetic iron and diamagnetic myelin, within the imaging voxel. The paramagnetic and diamagnetic susceptibility effects may partly or entirely cancel each other out, yielding a voxel-averaged susceptibility value and inaccurate quantification. Thus, developing a new imaging technique to quantify iron and myelin throughout the whole brain regions is essential. A few studies have attempted to separate paramagnetic susceptibility proportion from diamagnetic susceptibility (Chen et al., 2021; Shin et al., 2021). The recently proposed APART-QSM has demonstrated an improved performance for simultaneously quantifying brain iron and myelin by employing a comprehensive complex data model and iterative voxel-wise magnitude decay kernel estimating algorithm (Z. Li et al., 2023). However, the developmental trajectories of both paramagnetic and diamagnetic susceptibility as a function of age and their association remain to be elucidated.

In this study, we assessed the sub-voxel magnetic susceptibility of the human brain in vivo ranging from aged 18 to 80 years. First, we developed longitudinal and age-specific atlases of paramagnetic and diamagnetic susceptibility, serving as templates for normative brain iron accumulation and myelin development across adulthood. Furthermore, we quantified the developmental trajectories of paramagnetic and diamagnetic susceptibility in various brain regions to characterize the age-related iron and myelin alternations, particularly myelin in deep gray matter (DGM) and iron in WM. Our findings revealed that myelination rates varied among DGM nuclei. Moreover, in the major WM fiber bundles, the myelination process was accompanied by a complementary trend of iron accumulation. Our goal is to offer a quantitative description of sub-voxel magnetic susceptibility changes associated with brain aging. We anticipate that this understanding will enable us to gain deeper insights into potential abnormalities of magnetic susceptibility arising from various neurological diseases and neural degeneration. In particular, examining alterations in paramagnetic and diamagnetic susceptibility within the same voxel during normal brain aging and their potential relationships could provide a reference for evaluating brain demyelination and iron deposits in diseased brains.

## 2 | METHODS

### 2.1 | Data acquisition

A total of 494 subjects (age 18–80, 244M/250F, Cohort 1) were included in the analysis study. The subjects were scanned using a 3T MR scanner (uMR790, United Image Healthcare (UIH), Shanghai, China). The 3D multi-echo gradient echo (GRE) sequence was utilized

to reconstruct the susceptibility map and estimate  $R_2^*$  map. T1-weighted (T1w) images were acquired using a magnetization prepared rapid acquisition gradient echo (MPRAGE) sequence. The acquisition protocols of both sequences are listed in Table 1.

Another 13 subjects (age 23–29, 7M/6F, **Cohort 2**) were recruited and scanned at the same MR scanner as used for the data acquisition of **Cohort 1**. The protocols of 3D multi-echo GRE and 2D multi-echo spin echo (SE) sequences were conducted to acquire  $R_2^*$  and  $R_2$  maps (Table 2). These maps were utilized to estimate the essential  $R_2'$  map for susceptibility separation in **Cohort 1**. In addition,

32 subjects (age 4–39, 22M/10F, **Cohort 3**) were scanned at Shanghai Ruijin Hospital using a UIH 3T MR scanner (uMR890, UIH, Shanghai, China). The 3D multi-echo GRE and 2D multi-echo SE sequences were also scanned for precise susceptibility separation and the fitting of developmental trajectory in **Cohort 3**. Additionally, this fitted developmental trajectory was compared with the susceptibility trajectories derived from the data in **Cohort 1**.

## 2.2 | Image preprocessing

$R_2^*$  and  $R_2$  maps were estimated using a mono-exponential fitting of the magnitude at different echo times of the multi-echo GRE data and multi-echo SE data, respectively. The first echo of multi-echo SE was excluded for fitting  $R_2$  maps because of the different components of the first echo with respect to the other echoes (Biasioli et al., 2013). For QSM reconstruction, the raw phase of multi-echo GRE data was first unwrapped using a Laplacian-based phase unwrapping method (Schofield & Zhu, 2002). The tissue phase was extracted from the unwrapped phase using V-SHARP method (W. Li, Avram, et al., 2014; Wu et al., 2012). Then susceptibility maps were derived based on STAR-QSM (Wei et al., 2015).

Each individual T1w image was rigidly co-registered to the first echo of the multi-echo GRE magnitude image using the advanced normalization tools (ANTs) (Avants et al., 2010). The intensity of the co-registered T1w image was then rescaled to 0–255. Using the

**TABLE 1** The acquisition protocols of **Cohort 1**.

Sequence	3D multi-echo GRE	MPRAGE
TR (ms)	34.6	8.1
Echo number	8	1
TE <sub>1</sub> /spacing/TE <sub>last</sub> (ms)	3.3/3.7/29.2	3.4
Readout mode	Bipolar	N/A
TI (ms)	N/A	1060
Flip angle (°)	15	8
Bandwidth (Hz/pixel)	280	260
Matrix size	318 × 336 × 74	208 × 300 × 250
Spatial resolution (mm)	0.65 × 0.65 × 2	0.8 × 0.8 × 0.8
Parallel imaging	GRAPPA ×2	GRAPPA ×2
Scan time (min)	8.8	5.3

**TABLE 2** The acquisition protocols and the age information of **Cohort 2** and **Cohort 3**.

		Cohort 2	Cohort 3
Age (years)		23–29	4–39
3D multi-echo GRE	TR (ms)	34.6	40
	Echo number	6	7
	TE <sub>1</sub> /spacing/TE <sub>last</sub> (ms)	4.5/4.5/26.8	2.4/4.3/28.2
	Readout mode	Bipolar	Bipolar
	Flip angle (°)	15	8
	Bandwidth (Hz/pixel)	300	350
	Matrix size	240 × 240 × 80	224 × 224 × 80
	Spatial resolution (mm)	1 × 1 × 2	1.03 × 1.03 × 2
	Parallel imaging	GRAPPA ×2	GRAPPA ×2
	Scan time (min)	7.4	8.7
2D multi-echo SE	TR (ms)	4013	3864
	Echo number	4	5
	TE <sub>1</sub> /spacing/TE <sub>last</sub> (ms)	16.7/16.7/66.8	16.1/16.1/80.5
	Bandwidth (Hz/pixel)	160	160
	Matrix size	240 × 240 × 80	224 × 224 × 80
	Spatial resolution (mm)	1 × 1 × 2	1.03 × 1.03 × 2
	Parallel imaging	GRAPPA ×2	GRAPPA ×2
	Scan time (min)	17.8	16.1

normalized T1w images and reconstructed QSM images, the QSM(T1w) hybrid images were generated following Equation (1):

$$\text{QSM(T1w)} = \mu * \text{T1w} - \text{QSM} \quad (1)$$

where  $\mu$  is a weighting variable and empirically set to 0.0025 (Y. Zhang et al., 2018). The QSM(T1w) hybrid images preserve both the strong anatomical contrast of DGM nuclei in QSM and the clear cortical gray and white matter boundaries in the T1w image, which were used for the following atlas construction.

### 2.3 | Separation of paramagnetic and diamagnetic susceptibility

In this study, the paramagnetic and diamagnetic susceptibility mapping were reconstructed using the recently proposed method APART-QSM (Z. Li et al., 2023). Briefly, the APART-QSM employed a comprehensive complex data model on the raw GRE signal:

$$S(t) = M_0 e^{-(R_2 + a|\chi_{para}| + a|\chi_{dia}|)t} \cdot e^{i(\phi_{res} + \phi_{bg}(t) + 2\pi\gamma B_0(D * (\chi_{para} + \chi_{dia})))t} \quad (2)$$

where  $\chi_{para}$  is the paramagnetic susceptibility,  $\chi_{dia}$  is the diamagnetic susceptibility,  $\phi_{res}$  represents the time-independent residual phase,  $\phi_{bg}$  represents an echo time-dependent background phase,  $D$  is the magnetic dipole kernel and  $*$  denotes the spatial convolution. Specifically,  $a$  is the magnitude decay kernel, which is a proportionality constant between  $R'_2 (= R_2^* - R_2)$  and absolute susceptibility sources. APART-QSM utilized an iterative algorithm to solve the optimization problem and estimate the voxel-wise parameter  $a$ -map.

The estimation of  $R_2$  map typically acquired using a multi-echo SE, which is time-consuming. Previous studies assumed that  $R_2^*$  was

approximately proportional to the magnitude of susceptibility sources in the approximation of small concentrations (Dimov et al., 2022). In this study, we proposed a linear model to represent the magnitude of susceptibility source concentration and  $R_2^*$ . Specifically,  $R_2^*$  can be expressed as a first-order approximation of the reversible relaxation rate  $R'_2$ :

$$R_2^* = \alpha R'_2 + \beta \quad (3)$$

where  $\alpha$  and  $\beta$  are the slope and intercept estimated from the linear least-squares regression between mean  $R_2^*$  and  $R'_2$  value of five iron-rich deep nuclei ROIs in **Cohort 2**, including caudate nuclei (Cau), putamen (Pu), globus pallidus (GP), substantia nigra (SN) and red nuclei (RN). The approximated  $\widehat{R'_2}$  can be calculated according to Equation (3):

$$\widehat{R'_2} = (R_2^* - \beta) / \alpha \quad (4)$$

With the approximated  $\widehat{R'_2}$  map, APART-QSM can be used to reconstruct paramagnetic and diamagnetic susceptibility maps based on the GRE data in **Cohort 1**. We assume the bias induced by the estimated  $\widehat{R'_2}$  map to the final susceptibility separation results could be absorbed by the magnitude decay kernel  $a$ , which is intrinsically determined using an iterative algorithm in APART-QSM. As for the separation of paramagnetic and diamagnetic susceptibility in **Cohort 2** and **Cohort 3**, we directly applied APART-QSM since  $R'_2$  map is available.

### 2.4 | Atlas construction

The subjects in **Cohort 1** were divided into 6 groups by age intervals. Figure 1 shows the number of subjects and sex distribution at each age interval. Based on the QSM(T1w) hybrid images, a similar two-

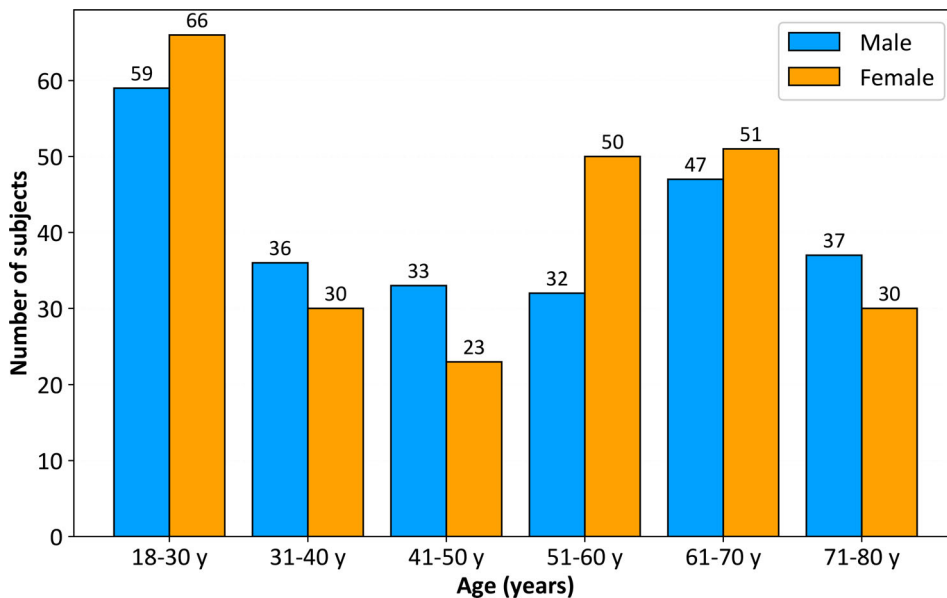


**FIGURE 1** The number of subjects at each age interval for atlas construction and statistical analysis.

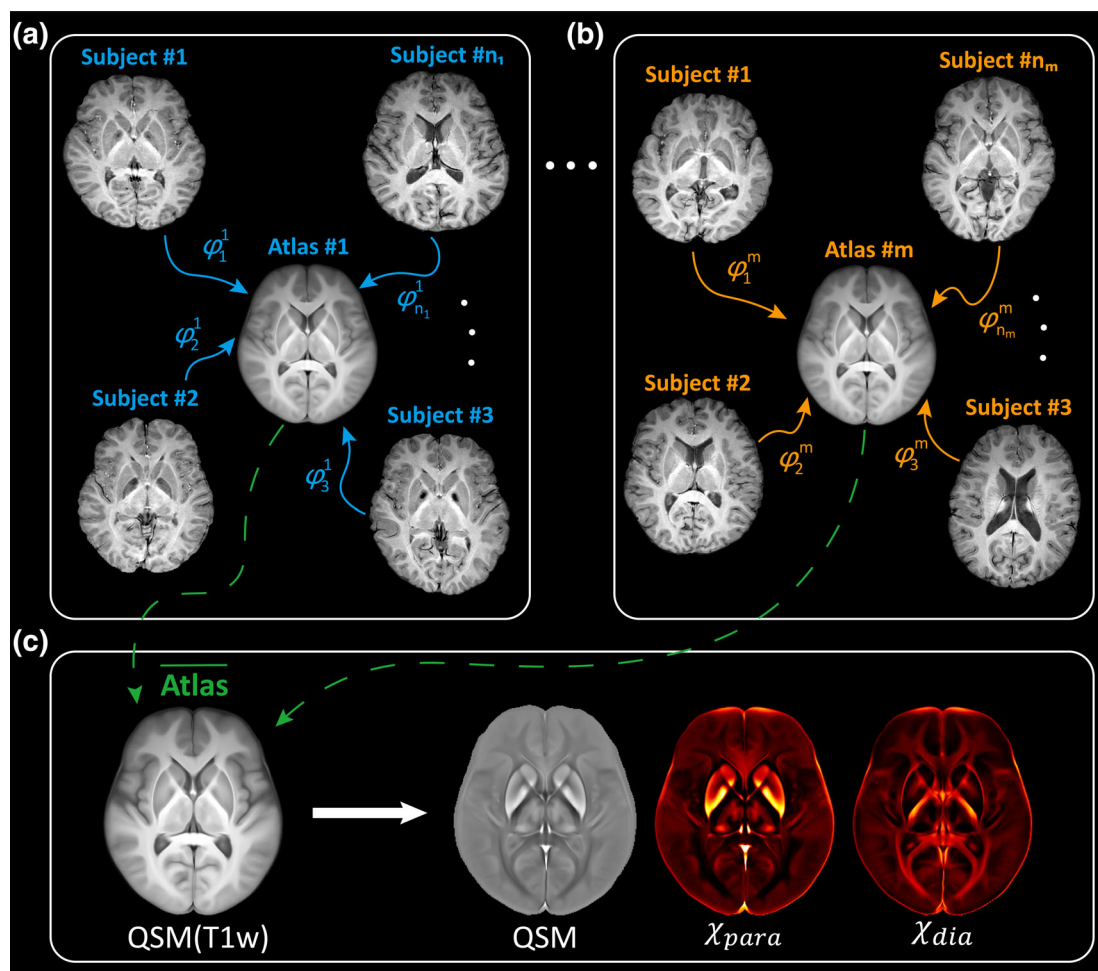


**FIGURE 2** The outline of two-step registration for atlas construction. (a, b) The group-wise registration was conducted to generate the age-specific atlas for each age interval (blue: the first age interval; orange: the  $m$ th age interval).  $\phi_i^j$  represents the transformation from the  $i$ th individual subject in the  $j$ th group toward the  $j$ th age-specific atlas and  $n_j$  represents the number of subjects in the  $j$ th group. (c) A longitudinal registration was conducted on the age-specific atlases to generate the longitudinal atlas of QSM(T1w) and the corresponding transformations (dashed line). The longitudinal atlases of QSM, paramagnetic susceptibility ( $\chi_{para}$ ) and diamagnetic susceptibility ( $\chi_{dia}$ ) were constructed by applying the two-step transformations.

step registration strategy (Y. Zhang et al., 2018) was employed, as shown in Figure 2. First, the group-wise registration was performed using ANTs within each age group to generate an age-specific atlas. Next, the longitudinal registration was applied to co-register each age-specific atlas to the MuSus-100 atlas (C. He et al., 2022) in Montreal Neurological Institute (MNI) space. The transformations from these two steps were respectively applied to the individual QSM, paramagnetic and diamagnetic susceptibility images to produce the longitudinal and age-specific atlas of different modalities. The constructed longitudinal atlases for paramagnetic and diamagnetic susceptibility are also publicly available at <https://github.com/AMRI-Lab/SubVoxel-QSM-Atlas>.

Moreover, the whole brain parcellation map was created based on the longitudinal atlas of T1w. To obtain the parcellation map in WM and cortex, the JHU DTI-based white-matter atlas (Mori et al., 2005) and AAL3 atlas (Rolls et al., 2020) in MNI space were rigidly registered to the MuSus-100 atlas to ensure the same spatial resolution. Subsequently, the whole brain parcellation map was formed

by combining the MuSus-100 atlas, the warped JHU DTI-based white-matter atlas and the warped AAL3 atlas.

## 2.5 | Statistical analysis

In order to perform ROI-based statistical analysis, the individual ROIs segmentation was achieved by applying the inverted transformations generated in Section 2.4. The mean susceptibility of each ROI in the individual space was calculated for further analysis.

The progression of the iron deposition and myelin development were both investigated in DGM and WM over the lifespan. In brain nuclei, the progressive accumulation of iron with aging has been reported to follow the exponential growth model (Hallgren & Sourander, 1958). As iron is the main source of susceptibility in DGM, the susceptibility can be fitted with the following three-parameter exponential equation:



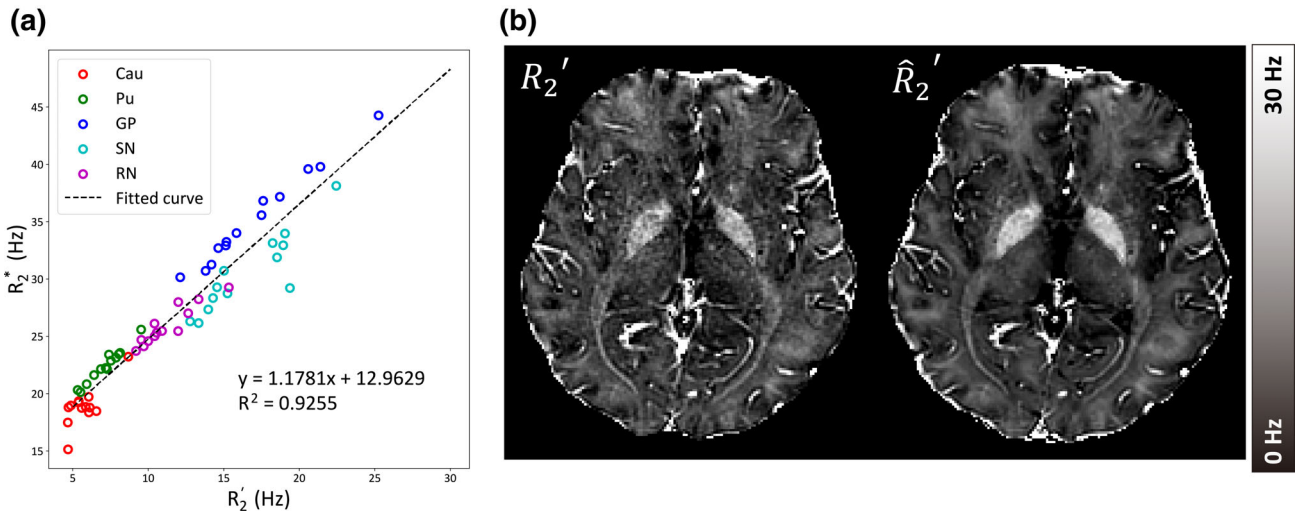


**FIGURE 3** The first-order approximation of  $R_2'$  map. (a) Linear regression between  $R_2'$  and  $R_2^*$ . (b) Qualitative comparison between  $R_2'$  and the approximated  $\widehat{R_2^*}$  map.

$$\chi = \alpha(1 - \exp(-\beta * age)) + \gamma \quad (5)$$

where  $\chi$  represents the magnetic susceptibility,  $\alpha$ ,  $\beta$ , and  $\gamma$  are tissue-specific parameters. In contrast, several nonlinear models have been proposed to fit the evolution of myelin in WM with aging, including quadratic (Hasan et al., 2009) and Poisson (Lebel et al., 2012) functions. In this work, we used the three-parameter Poisson function (W. Li, Wu, et al., 2014) to model the asymmetrical behavior of susceptibility developmental trajectories in WM:

$$\chi = A * age * \exp(-age/B) + C \quad (6)$$

where  $A$ ,  $B$ , and  $C$  are tissue-specific parameters. It is worth noting that  $B$  represents the age when the susceptibility value reaches its minimum. To model the myelin development in DGM and iron deposition in WM over the lifespan, we employed generalized additive models (GAMs) to flexibly capture the linear and nonlinear pattern of development (Larsen et al., 2020). To evaluate the accuracy of developmental trajectories, the same fitting procedure was conducted on **Cohort 3** aged from 4 to 39 years as well. Two developmental trajectories of magnetic susceptibility from **Cohort 1** and **Cohort 3** were compared.

The curve fitting was conducted using the optimization toolbox of Scipy (Virtanen et al., 2020). All data processing and computing procedures were implemented in Python 3.9 on a workstation with an Intel Core i7-11700 CPU and 64 GB RAM.

### 3 | RESULTS

#### 3.1 | Feasibility of $\widehat{R_2^*}$ approximating $R_2'$

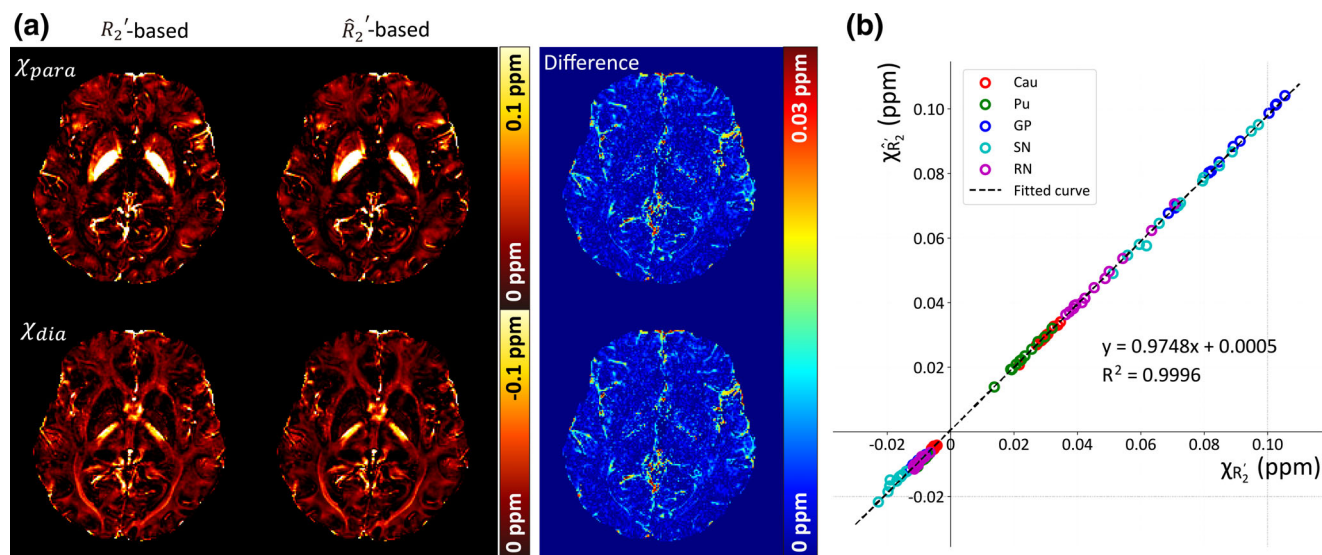
Figure 3 shows the validation of the first-order approximation of  $R_2'$  map estimated from  $R_2^*$  map. Figure 3a presents the linear regression

between  $R_2'$  and  $R_2^*$  within 5 DGM ROIs in **Cohort 2**. The resulting regression coefficients are  $\alpha = 1.1781$  and  $\beta = 12.9629$ , respectively ( $R^2 = 0.9255$ ,  $p < .001$ ). The representative slices of measured  $R_2'$  and the approximated  $\widehat{R_2^*}$  map exhibit a similar appearance, as illustrated in Figure 3b. To verify the feasibility of susceptibility separation based on  $\widehat{R_2^*}$  maps, Figure 4 presents the qualitative and quantitative comparison between the results of  $R_2'$ -based and  $\widehat{R_2^*}$ -based susceptibility separation. The paramagnetic susceptibility maps ( $\chi_{para}$ ), diamagnetic susceptibility maps ( $\chi_{dia}$ ) and their difference maps are displayed in Figure 4a. The difference maps indicate a minor difference of anatomical details in brain gray and white matters on  $\chi_{para}$  and  $\chi_{dia}$  maps. The large contrast difference mainly comes from the vessels due to the blooming artifacts on the  $R_2^*$  map. Quantitatively, the correlation analysis between the separated susceptibility values from the  $R_2'$ -based and  $\widehat{R_2^*}$ -based results demonstrate a good consistency with a coefficient of determination  $R^2 = 0.9996$  and a slope of 0.9748, as shown in Figure 4b.

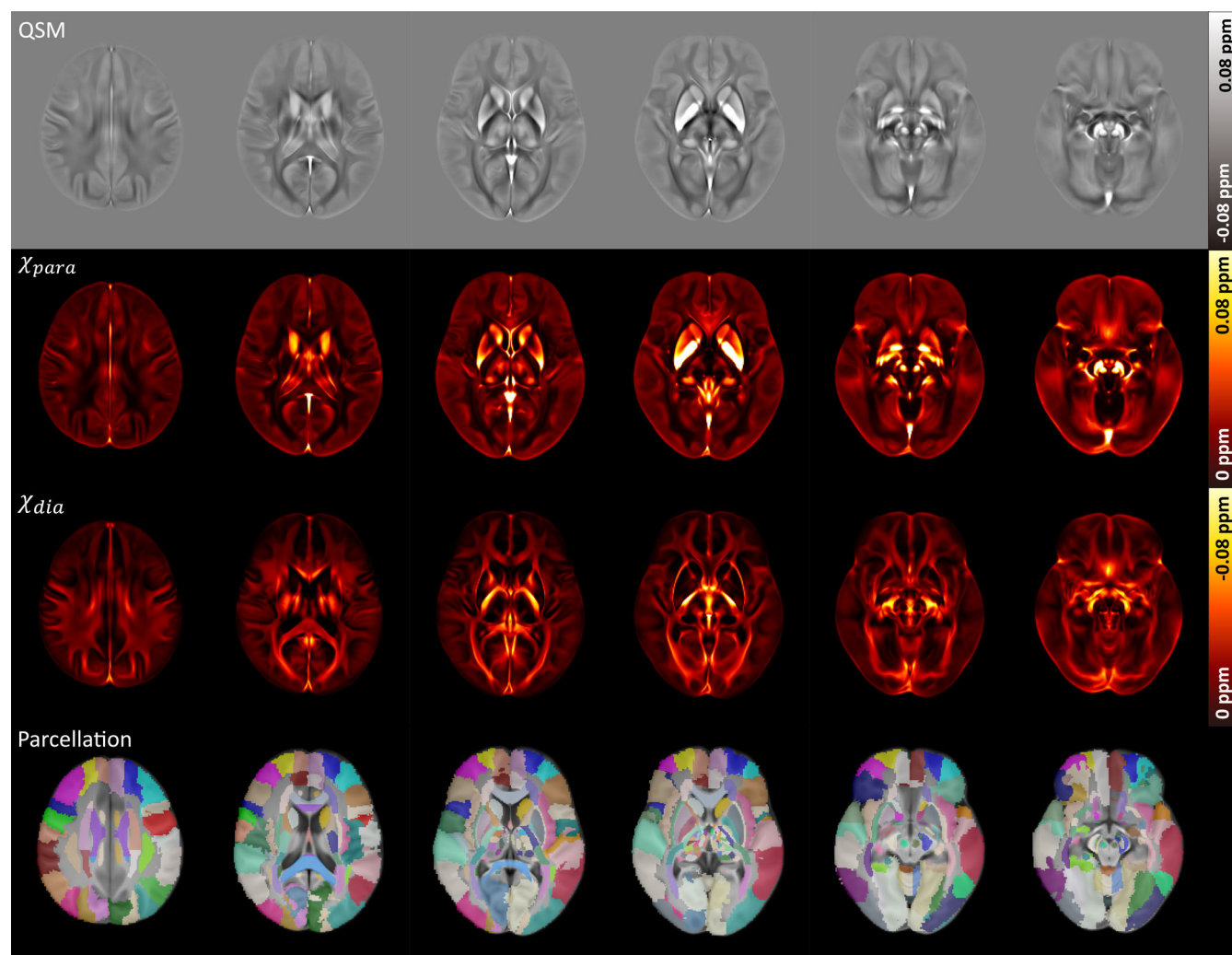
#### 3.2 | Atlas construction

Figure 5 displays six representative axial slices of the longitudinal brain atlases of QSM,  $\chi_{para}$  and  $\chi_{dia}$  constructed in **Cohort 1**. Although the longitudinal atlases are constructed from a large number of subjects across 18–80 years old, the atlases effectively preserve anatomical structures in DGM and the structural details in WM visually.

Figure 6 exhibits the zoomed-in views of the age-specific atlases within the basal ganglia and thalamus. The magnetic susceptibility of basal ganglia and thalamus varies diversely in different sub-regions. Compared to the magnetic susceptibility changes of QSM with age in Figure 6a, the separated  $\chi_{para}$  and  $\chi_{dia}$  maps can provide more accurate iron-related and myelin-related temporal variations with age. The magenta arrow in Figure 6b indicates that the paramagnetic



**FIGURE 4** The qualitative and quantitative comparison between the susceptibility separation results of APART-QSM based on  $R_2'$  and  $\hat{R}_2$  maps. (a) A representative slice of  $R_2'$  and  $\hat{R}_2$  based susceptibility separation and their difference maps. (b) Correlation analysis between separated susceptibility based on  $R_2'$  and  $\hat{R}_2$  maps over five ROIs in Cohort 2.



**FIGURE 5** The representative slices of longitudinal atlases of QSM,  $\chi_{para}$ , and  $\chi_{dia}$  from the first row to the third row. The fourth row displays the whole brain parcellation map formed by combining the MuSus-100 atlas, the warped JHU DTI-based white-matter atlas and the warped AAL3 atlas.



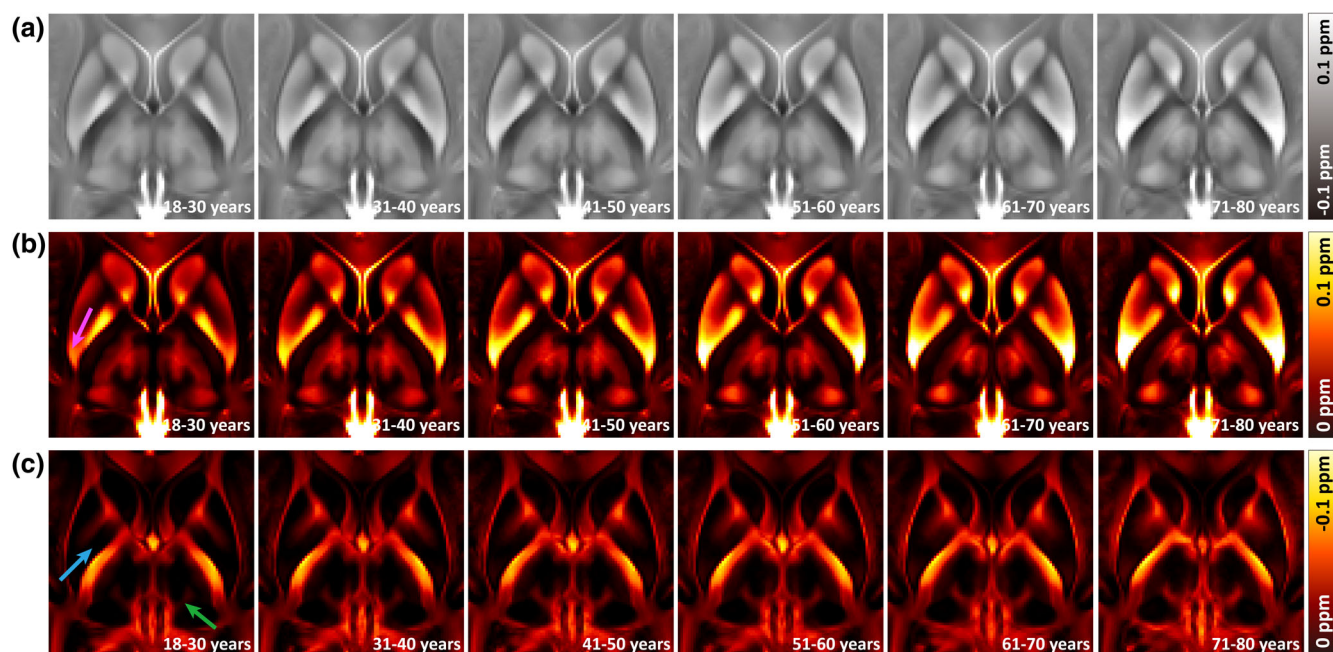


**FIGURE 6** Age-specific atlases of QSM,  $\chi_{para}$  and  $\chi_{dia}$  within the basal ganglia and thalamus from top to bottom. The paramagnetic susceptibility of Pu increases with aging (magenta arrow). The diamagnetic susceptibility of GP (blue arrow) and internal medullary lamina (green arrow) decrease with aging.

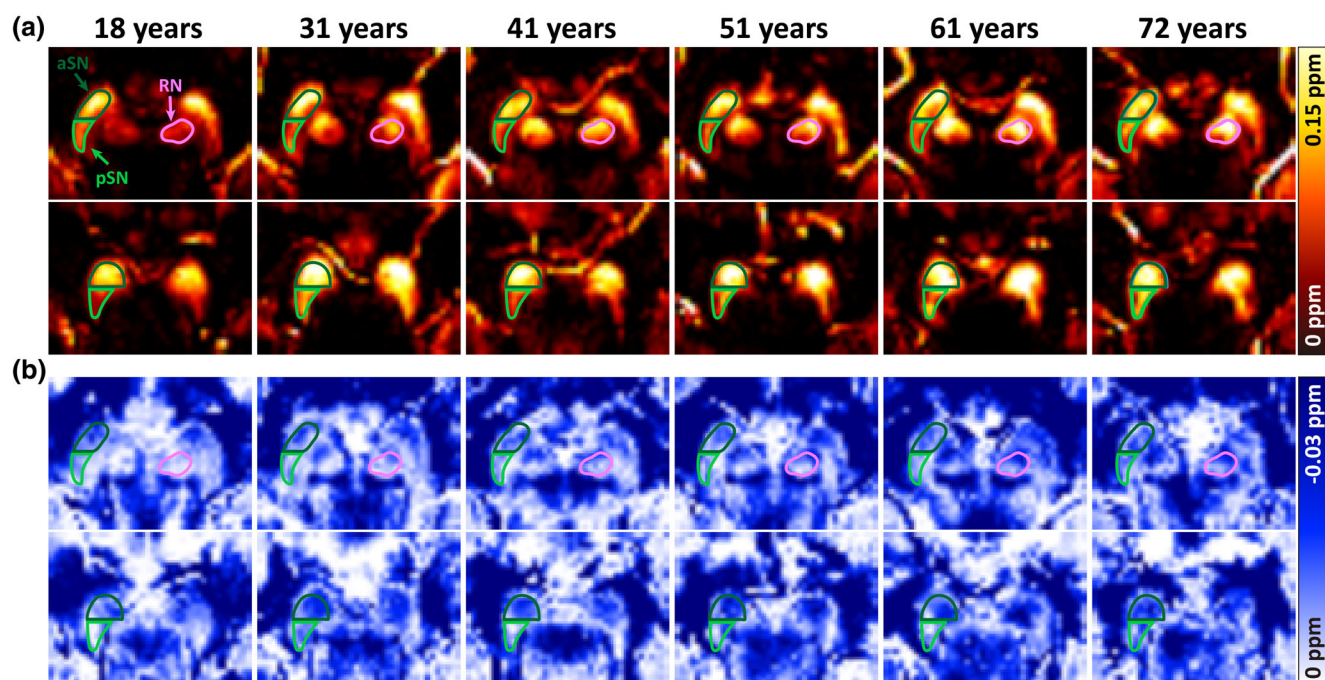


**FIGURE 7** Evolution of susceptibility with aging in SN and RN. (a) The  $\chi_{para}$  maps of the individual subjects at each age interval. The upper and lower rows show the rostral level and caudal level of SN, respectively. (b) The  $\chi_{dia}$  maps of individual subjects. aSN, anterior substantia nigra (dark green arrow); pSN, posterior substantia nigra (light green arrow); RN, red nuclei (pink arrow).

susceptibility in Pu obviously increases with aging. The blue arrow in Figure 6c points to the developments of diamagnetic susceptibility in GP, which becomes more diamagnetic with aging. This variation is not possible to obtain based on traditional QSM due to the averaged

opposing susceptibility values in a single voxel. In addition, the susceptibility of the internal medullary lamina in the thalamus (green arrow) becomes more diamagnetic with aging, which is also not obvious on traditional QSM images.



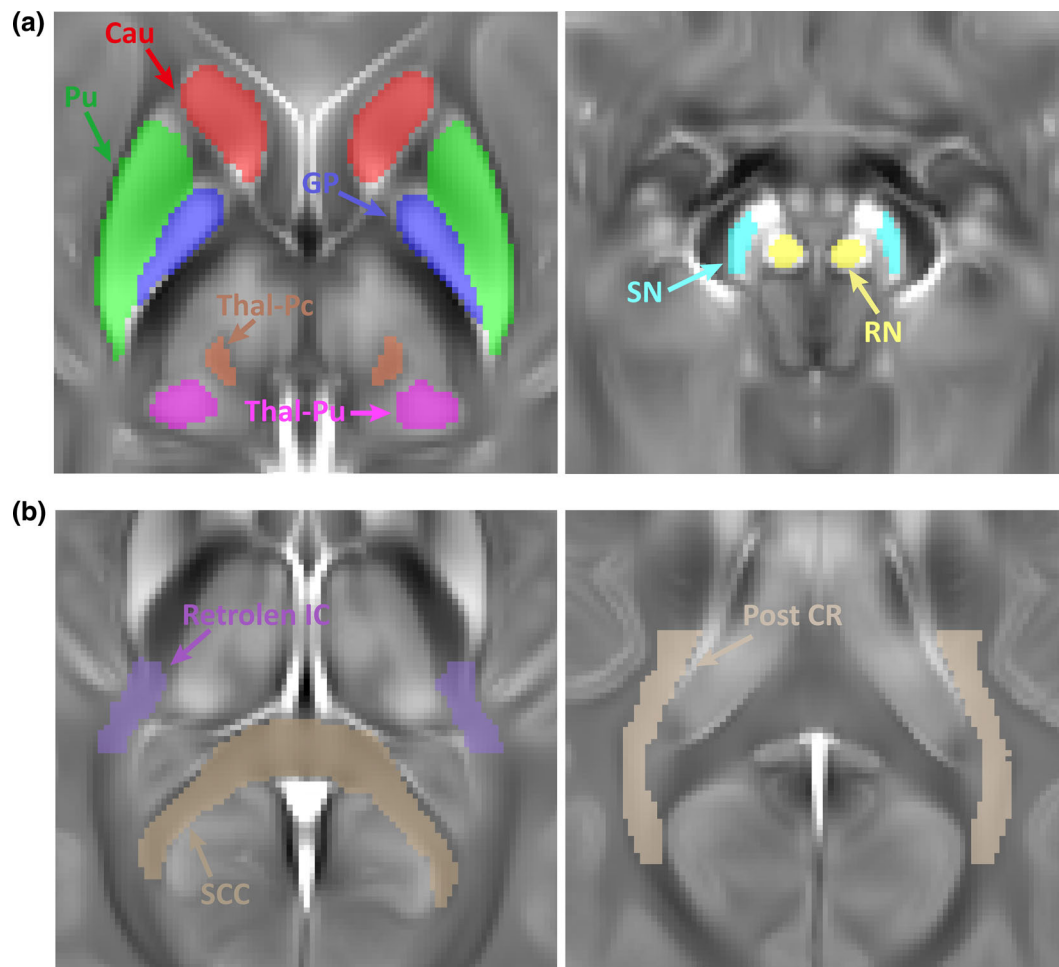


**FIGURE 8** The representative ROIs in DGM and WM. (a) The DGM ROIs include caudate nuclei (Cau), putamen (Pu), globus pallidus (GP), substantia nigra (SN) and red nuclei (RN). The thalamus sub-region ROIs include thalamus paracentral (Thal-Pc) and pulvinar thalami (Thal-Pu). (b) The WM ROIs include the retrolenticular internal capsule (Retrolen IC), splenium of the corpus callosum (SCC) and posterior corona radiata (Post CR).

### 3.3 | Individual susceptibility variations within small deep gray matter nuclei

Figure 7 displays the  $\chi_{para}$  and  $\chi_{dia}$  maps of each age interval at two representative axial locations, covering SN and RN. The individual images were all registered to the common space of the longitudinal atlas by applying the corresponding transformations. The anterior SN (aSN) and posterior SN (pSN) were defined by splitting the SN ROI along the line of the anterior-posterior axis. The pink arrow in Figure 7a indicates an obvious  $\chi_{para}$  increasing with aging in RN. Additionally, the heterogeneity of  $\chi_{para}$  is observed in SN with slightly higher susceptibility in aSN (dark green arrow) than pSN (light green arrow). This obvious anteroposterior gradient of iron between aSN and pSN is consistent with a previous postmortem validation (Massey & Yousry, 2010). In Figure 7b, it is observed that both the  $\chi_{dia}$  value at the rostral level (the first row) and the caudal level (the second row) of SN behave more diamagnetic with aging.

### 3.4 | Developmental trajectory of susceptibility across lifespan

Based on the parcellation maps of the MuSus-100 atlas (C. He et al., 2022) and the JHU DTI-based white-matter atlas (Mori et al., 2005), five DGM ROIs and three WM ROIs in MNI space are shown in Figure 8. Additionally, two sub-region ROIs in the thalamus were manually extracted based on the constructed longitudinal atlas. The inverted transformations in Section 2.4 were applied to generate the individual ROIs segmentation for the analysis of the susceptibility development with normal aging.

#### 3.4.1 | Trajectory of susceptibility development in deep gray matter

Figure 9 shows the developmental trajectories with aging in Cau. The trajectories of traditional susceptibility (Figure 9a,d) and

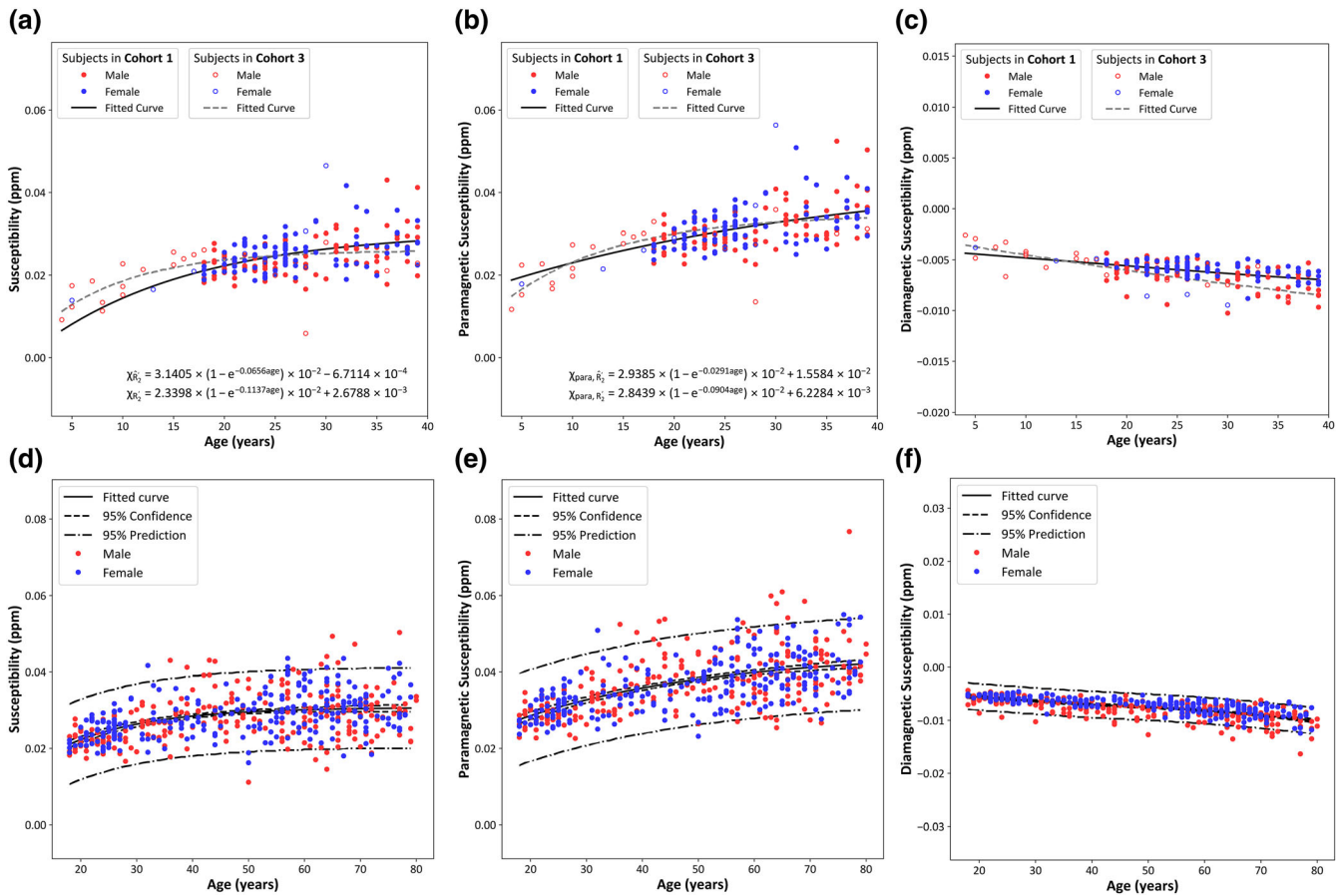


**FIGURE 9** The developmental trajectories of susceptibility with aging in Cau. (a–c) The comparison of QSM,  $\chi_{para}$  and  $\chi_{dia}$  trajectories in **Cohort 1** (the solid curves and closed circles) and **Cohort 3** (the dashed curves and open circles) from the age of 4 to 39. Red points: male, blue points: female. (d–f) The QSM,  $\chi_{para}$  and  $\chi_{dia}$  trajectory in **Cohort 1** over the adult lifespan. The solid, dashed and dash-dot curves represent the fitted trajectories, 95% confidence and prediction intervals, respectively.

paramagnetic susceptibility (Figure 9b,e) show an exponential-growth increase, while the diamagnetic susceptibility (Figure 9c,f) displays a slight decrease with aging. Due to the separation of  $\chi_{dia}$  at the sub-voxel level,  $\chi_{para}$  exhibits a faster increase rate than QSM. The paramagnetic susceptibility value rises rapidly during the first four decades of life and then reaches plateaus around the fifth decade, which is consistent with the results reported by Li et al. (W. Li, Wu, et al., 2014). Besides, the slight monotonic decrease of  $\chi_{dia}$  in Cau indicates the myelination process might continue throughout the lifespan. In addition, the trajectories fitted in **Cohort 3** are compared with those in **Cohort 1** as shown in Figure 9a–c. The trajectories calculated from the two cohorts are roughly consistent, demonstrating the efficiency of  $\widehat{R}_2^2$ -based susceptibility separation using APART-QSM.

Figures 10 and 11 present the developmental trajectories in Pu and RN, respectively. Similar to the trajectory of Cau, the paramagnetic susceptibility in Pu and RN also follow the exponential growth model. Differently, susceptibility increases continuously at an approximately constant rate until the age of the 80s in Pu. The developmental trajectory of  $\chi_{dia}$  in Pu displays a rapid drop during the

first two decades then gradually approaches its plateau. In Figure 11c, the trajectory in **Cohort 1** slightly deviates from that in **Cohort 3** in RN.

The developmental trajectories of two sub-regions in the thalamus are displayed in Figures 12 and 13. In Thal-Pu, the trajectories of  $\chi_{para}$  follow the exponential growth model, revealing continuous iron accumulation with aging in the thalamic nuclei (Figure 12b,e). Interestingly, the  $\chi_{dia}$  in Thal-Pu (Figure 12c,f) remains constant over the lifespan. In comparison, the development of  $\chi_{dia}$  in Thal-Pc exhibits continuous decrease with aging (Figure 13c,f) whereas  $\chi_{para}$  displays no obvious variation throughout the lifespan (Figure 13b,e). The sex difference of the developmental trajectories in DGM is presented in Figures S7–S13.

### 3.4.2 | Trajectory of susceptibility development in white matter

Figures 14–16 show the susceptibility evolutions in three white matter regions, including Retrolen IC, SCC and Post CR. The developmental

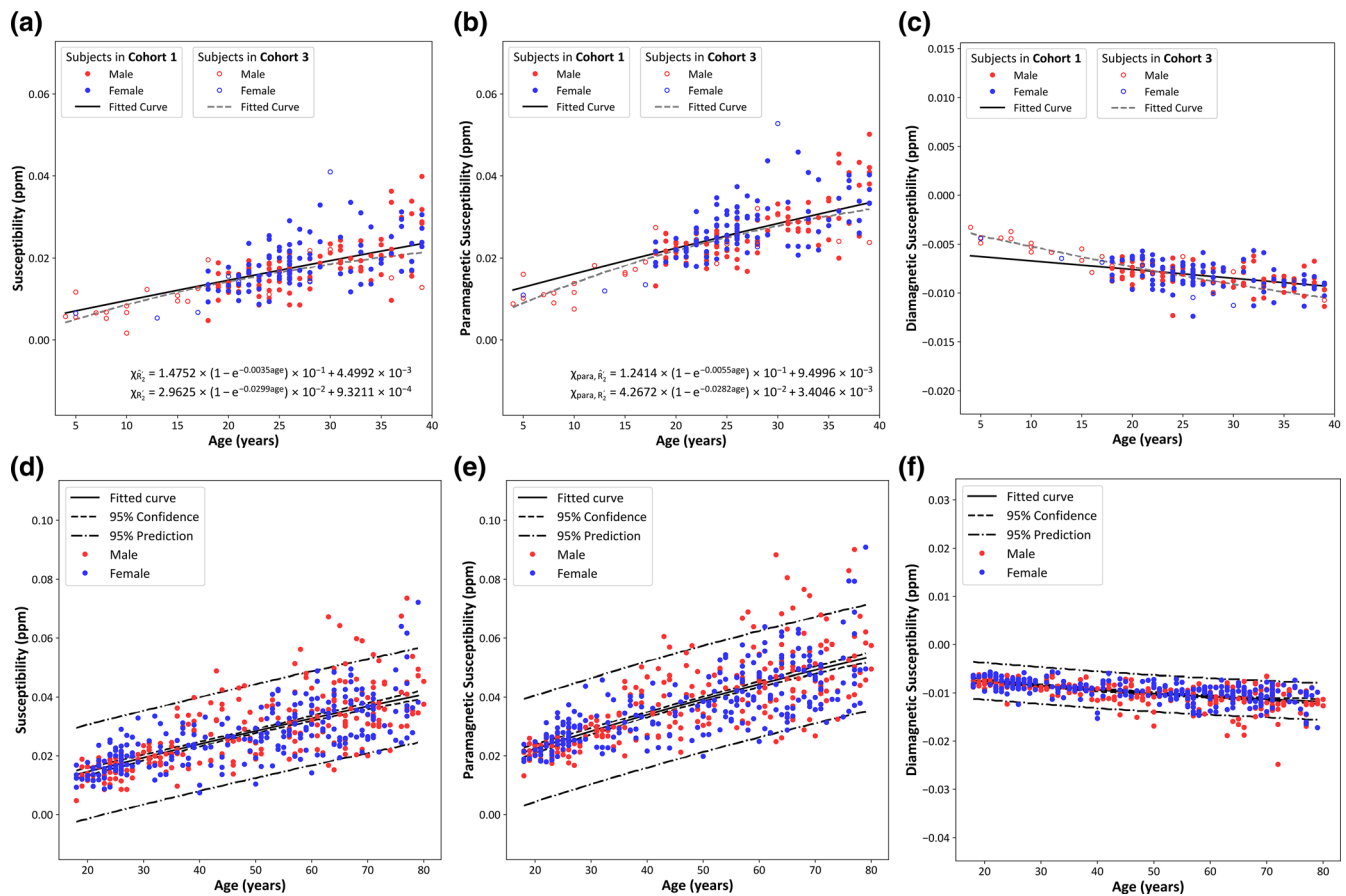


**FIGURE 10** The developmental trajectories of susceptibility with aging in Pu. (a–c) The comparison of QSM,  $\chi_{para}$  and  $\chi_{dia}$  trajectories in **Cohort 1** (the solid curves and closed circles) and **Cohort 3** (the dashed curves and open circles) from the age of 4 to 39. Red points: male, blue points: female. (d–f) The QSM,  $\chi_{para}$  and  $\chi_{dia}$  trajectory in **Cohort 1** over the adult lifespan. The solid, dashed and dash-dot curves represent the fitted trajectories, 95% confidence and prediction intervals, respectively.

trajectories calculated based on the traditional QSM remain stable over the lifespan in Figure 14a,d. However, the  $\chi_{dia}$  first becomes more diamagnetic as the brain matures and then increases monotonically with aging, as shown in Figure 14c,f. Therefore, the fitted Poisson trajectory of  $\chi_{dia}$  is consistent with the asymmetrical behavior of white matter, as reported by DTI studies (Lebel et al., 2012). In Retrolen IC (Figure 14),  $\chi_{dia}$  reaches its peak diamagnetic value at around 44 years of age, which is similar to the fitted model parameters in the previous study (W. Li, Wu, et al., 2014). In SCC (Figure 15),  $\chi_{dia}$  decreases rapidly in the first decade, gradually slows down and reaches its minimum at around 39 years of age. In comparison, susceptibility in the white matter of Post CR (Figure 16) reaches its minimum at roughly 44 years of age.

Iron deposition in the white matter has been found to be essential for the development of myelin (Algarin et al., 2003). Therefore, the investigation of the development of  $\chi_{para}$  in white matter is also of great significance. Our results show that the evolutions of  $\chi_{para}$  in Retrolen IC (Figure 14b,e) exhibit significant increases during the first four decades, then trend to decrease. It is worth noting that the

trajectories of  $\chi_{para}$  and  $\chi_{dia}$  in Retrolen IC (Figure 14e,f) show the complementary trend, that is,  $\chi_{para}$  becomes more paramagnetic while  $\chi_{dia}$  becomes more diamagnetic in the same WM region from the age of 4 to about 40 years. This may imply the essential role of iron deposition for WM myelination in this area. In contrast, the developmental trajectory of  $\chi_{para}$  remains stable in SCC (Figure 15b,e). The sex difference of the developmental trajectories in WM is presented in Figures S14–S20.

## 4 | DISCUSSION

In this study, we assessed the sub-voxel magnetic susceptibility across various brain structures ranging from 18 to 80 years old in a cohort of 494 healthy adults. Based on the assumption that  $R_2^*$  can be estimated as the first-order approximation of  $R_2^*$ , the susceptibility separation method (Z. Li et al., 2023) was performed on the GRE data to obtain the paramagnetic and diamagnetic susceptibility maps. Subsequently,

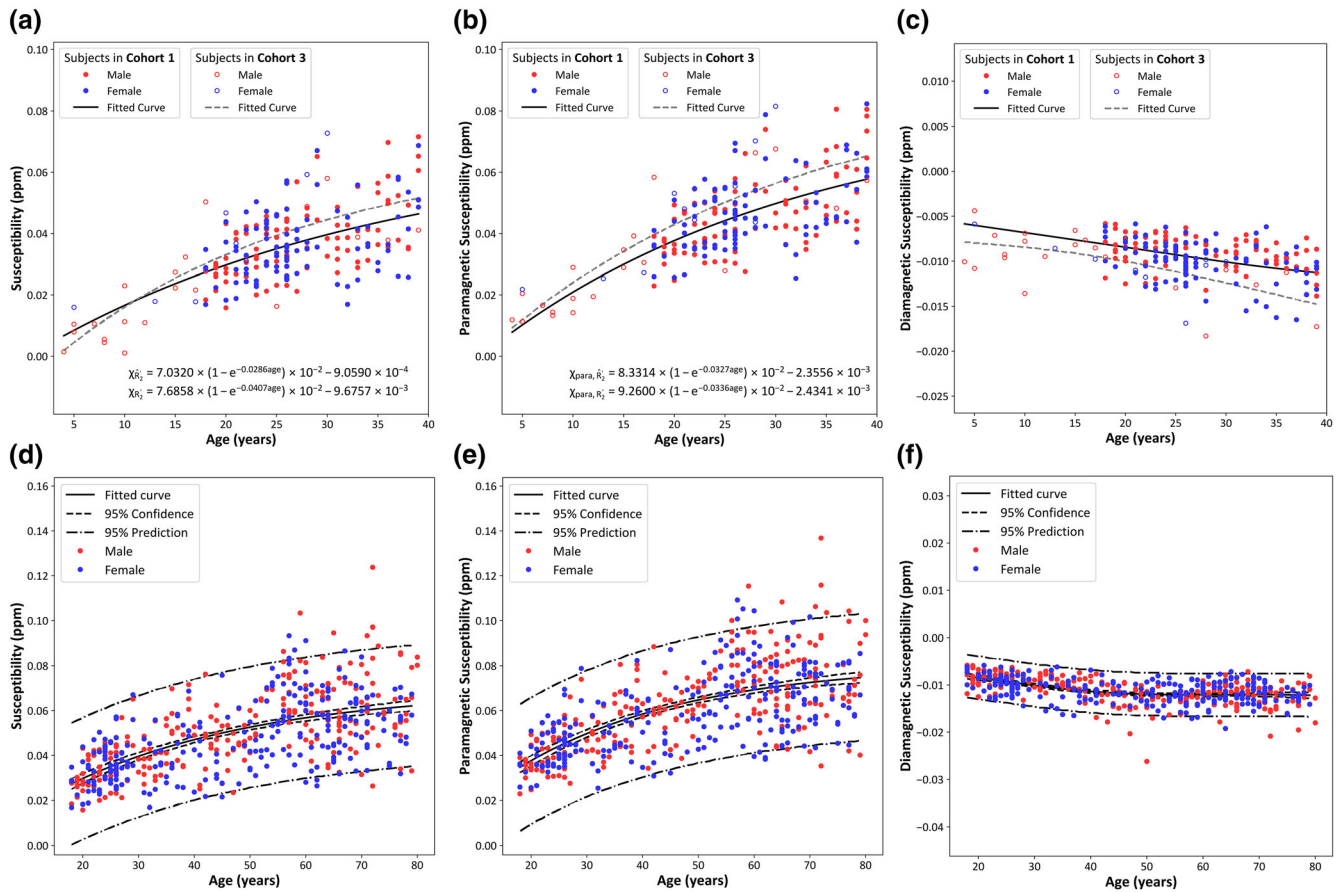


**FIGURE 11** The developmental trajectories of susceptibility with aging in RN. (a–c) The comparison of QSM,  $\chi_{para}$  and  $\chi_{dia}$  trajectories in **Cohort 1** (the solid curves and closed circles) and **Cohort 3** (the dashed curves and open circles) from the age of 4 to 39. Red points: male, blue points: female. (d–f) The QSM,  $\chi_{para}$  and  $\chi_{dia}$  trajectory in **Cohort 1** over the adult lifespan. The solid, dashed and dash-dot curves represent the fitted trajectories, 95% confidence and prediction intervals, respectively.

the longitudinal and age-specific atlases of QSM,  $\chi_{para}$  and  $\chi_{dia}$  were constructed. The age-specific atlases of  $\chi_{para}$  and  $\chi_{dia}$  can effectively reflect tissue susceptibility variations at each age interval, offering a valuable reference for investigating the development of brain gray and white matter with aging and for identifying deviations from a healthy population. We also investigated the developmental trajectories of paramagnetic and diamagnetic susceptibility simultaneously in various brain structures. The observed exponential growth trajectories corroborate the findings from previous studies (W. Li, Wu, et al., 2014) on paramagnetic susceptibility progression in iron-rich DGM nuclei. Additionally, the three-parameter Poisson equation fits well with the asymmetrical pattern observed in the evolution of diamagnetic susceptibility in the major WM fiber bundles. In addition, our results also reveal the developmental trajectories of  $\chi_{para}$  in WM and  $\chi_{dia}$  in DGM in vivo. Our results uncover, for the first time, the developmental synchrony between myelination and iron deposition in WM. These findings imply that age-dependent evolution of both paramagnetic and diamagnetic susceptibility, utilizing the proposed sub-voxel QSM method, may provide valuable

insights into the spatiotemporal patterns of myelination and iron accumulation during aging and neurodegenerations.

#### 4.1 | Iron and myelin development inferred from the trajectory of sub-voxel susceptibility

QSM has been extensively used to investigate the development of susceptibility in the iron-rich DGM nuclei and myelin-rich WM during brain maturation and aging (W. Li, Wu, et al., 2014; Treit et al., 2021; Y. Zhang et al., 2018), to reflect the change of iron deposition and myelination/demyelination within various brain regions. These studies suggested that the susceptibility change in DGM is consistent with the previous histochemical findings of iron deposition (Hallgren & Sourander, 1958), following the exponential growth model. Meanwhile, the asymmetrical development trend of susceptibility in WM is coincident with the age-related microstructural changes using diffusion tensor imaging (DTI) (Lebel et al., 2012). However, the



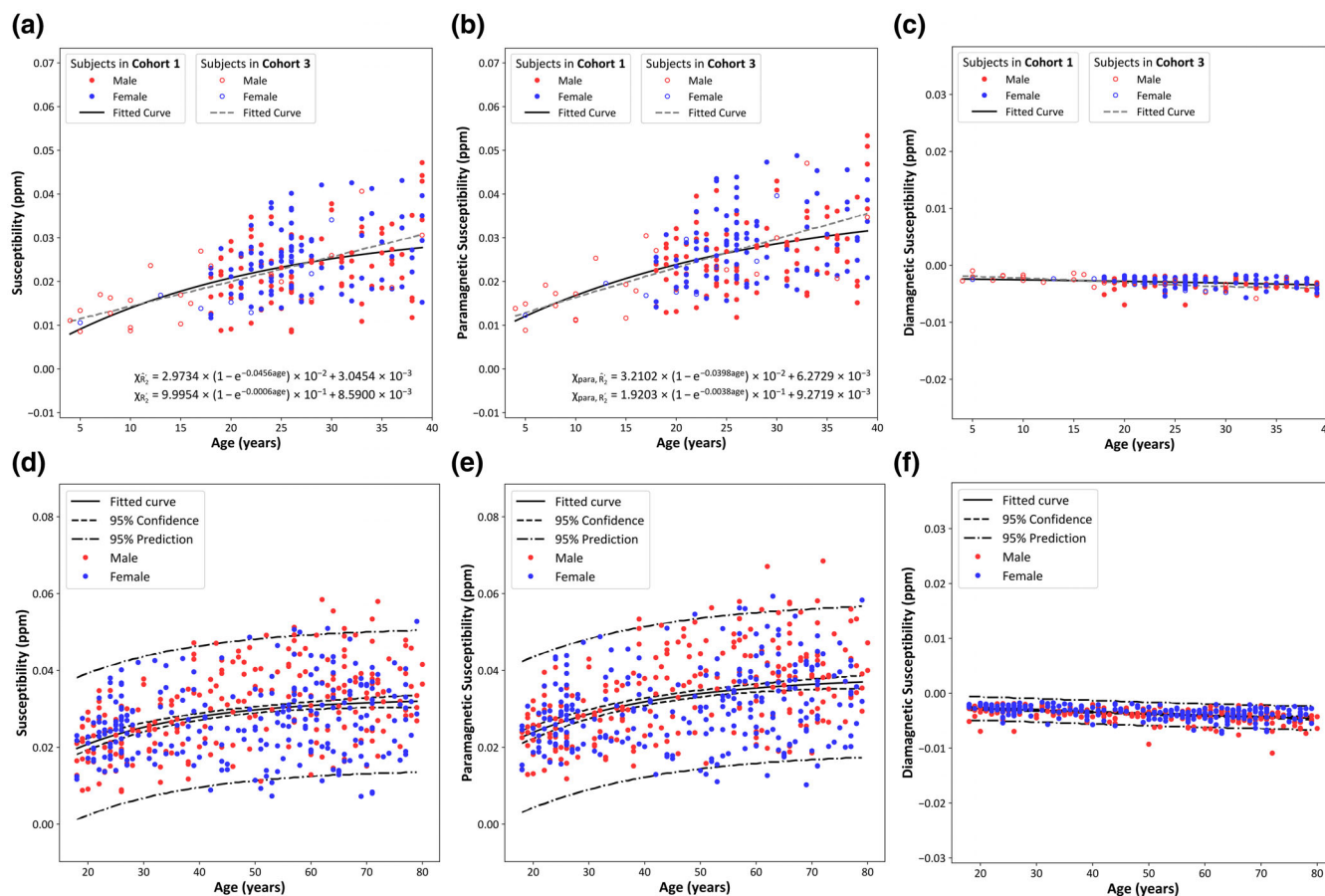


**FIGURE 12** The developmental trajectories of susceptibility with aging in Thal-Pu. (a–c) The comparison of QSM,  $\chi_{para}$  and  $\chi_{dia}$  trajectories in Cohort 1 (the solid curves and closed circles) and Cohort 3 (the dashed curves and open circles) from the age of 4 to 39. Red points: male, blue points: female. (d–f) The QSM,  $\chi_{para}$  and  $\chi_{dia}$  trajectory in Cohort 1 over the adult lifespan. The solid, dashed and dash-dot curves represent the fitted trajectories, 95% confidence and prediction intervals, respectively.

conventional QSM technique can only provide the voxel-averaged susceptibility value from the mix of opposing susceptibility sources in a single voxel. Recently, several studies proposed sub-voxel QSM techniques to distinguish the contributions of intra-voxel paramagnetic and diamagnetic susceptibility sources and quantify these two opposing susceptibilities (Chen et al., 2021; Shin et al., 2021). In this study, we utilized APART-QSM (Z. Li et al., 2023), a promising susceptibility separation method, to investigate the developmental trajectories of QSM,  $\chi_{para}$  and  $\chi_{dia}$  simultaneously. With the advantage of sub-voxel QSM, the  $\chi_{para}$  and  $\chi_{dia}$  can be separately quantified and analyzed in the same region. Our results demonstrate that there is an obvious gap between the trajectories of  $\chi_{para}$  and QSM in most of the ROIs in DGM (Figures 9–11). This phenomenon arises from the underestimation of iron quantification in QSM due to the presence of myelinated axons in DGM (Naidich et al., 2012; Schaltenbrand & Wahren, 1977). Therefore, the trend of  $\chi_{para}$  provided a more accurate developmental trajectory of iron in DGM during brain maturation and aging. Similarly, our results reveal a biphasic temporal pattern of  $\chi_{dia}$  in

WM, with an initial decrease followed by an increase whereas QSM exhibited a plateau in certain WM regions (Figures 14 and 16). This trend coincides with the characteristic of myelin maturation and degradation during aging. Consequently, the trajectories of  $\chi_{dia}$  in WM have the potential to reveal a more accurate myelination or demyelination process compared to conventional QSM. In addition, we compared the developmental trajectories of males and females and observed minimal differences in most DGM and WM regions (Figures S7–S20). However, it is worth noting that within RN and Thal-Pu, we noticed a faster increasing rate of  $\chi_{para}$  in males, which may indicate a higher level of iron deposition with aging in these regions compared to females.

More importantly, our results show that the development of iron deposition in WM and myelination/demyelination in DGM in vivo can be quantified using sub-voxel QSM. We observed spatial variation in the diamagnetic susceptibility trajectories within DGM. For example, the developmental trajectories of  $\chi_{dia}$  in Pu and RN (Figures 10f and 11f) depict the myelination process in the

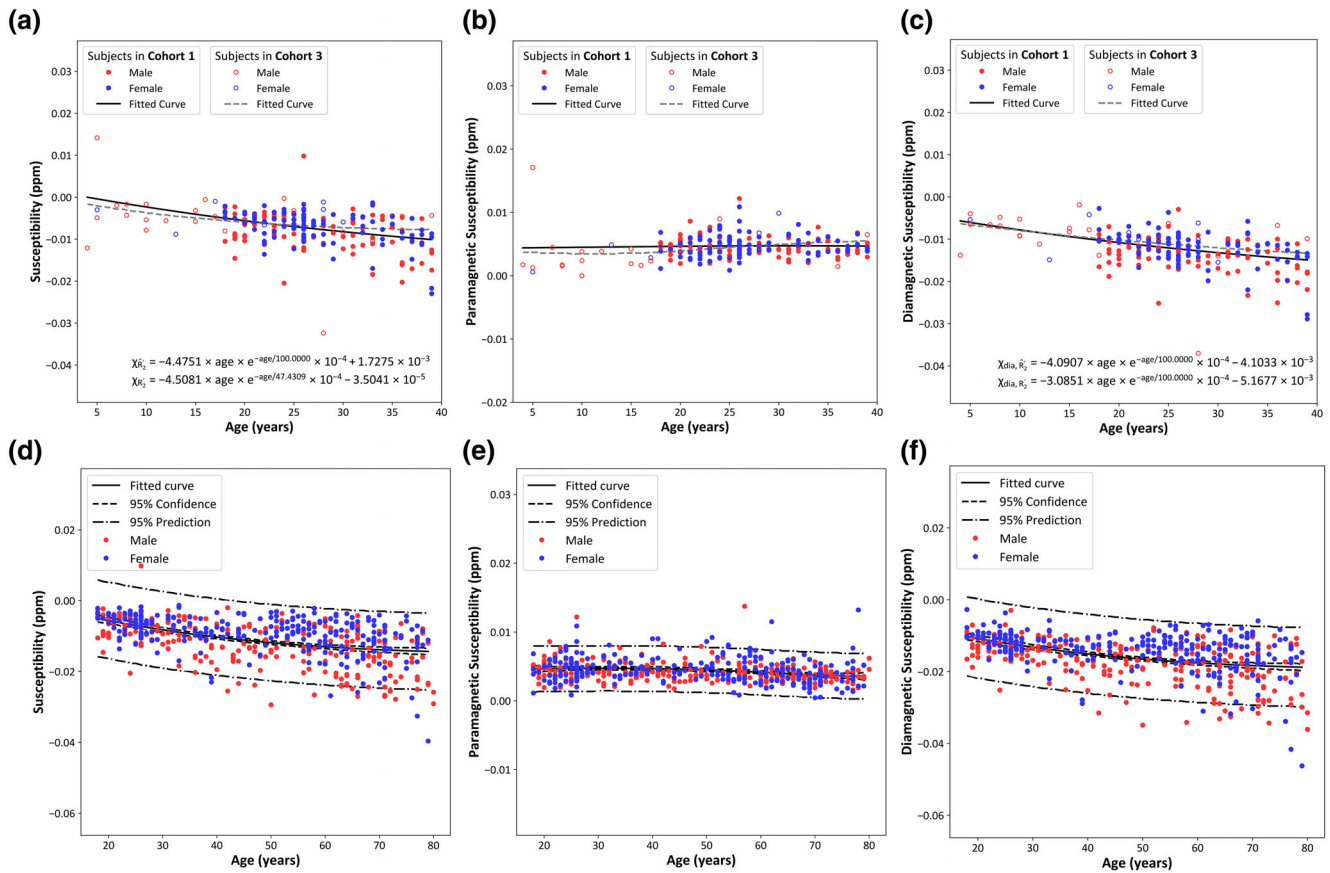


**FIGURE 13** The developmental trajectories of susceptibility with aging in Thal-Pc. (a–c) The comparison of QSM,  $\chi_{para}$  and  $\chi_{dia}$  trajectories in **Cohort 1** (the solid curves and closed circles) and **Cohort 3** (the dashed curves and open circles) from the age of 4 to 39. Red points: male, blue points: female. (d–f) The QSM,  $\chi_{para}$  and  $\chi_{dia}$  trajectory in **Cohort 1** over the adult lifespan. The solid, dashed and dash-dot curves represent the fitted trajectories, 95% confidence and prediction intervals, respectively.

first four decades followed by a plateau, while the trajectory of  $\chi_{dia}$  in Cau (Figure 9f) indicates a relatively slower trend of myelination throughout the lifespan. The different spatial patterns of the  $\chi_{dia}$  trajectories reflect a heterogeneous myelination process in the brain DGM nuclei. The impact of such heterogeneity on neural function during brain development remains unclear and warrants further investigation. Additionally, this finding holds the potential to enhance our comprehension of the pathology associated with various neurodegenerative disorders, such as Parkinson's disease (PD), Alzheimer's disease (AD) and multiple sclerosis (MS). A recent study demonstrated that QSM showed diverse discriminative power for health controls (HC) with PD in different SN subdivisions, attributable to the heterogeneous distribution of iron and myelin within SN (Lee et al., 2021). Our results (Figure 7b) depict the presence of increasing myelin in both rostral and caudal level of SN, contrasting with the inference in the previous study (Lee et al., 2021). Consequently, we could carry out the longitudinal investigation of iron accumulation and myelination in the whole SN using  $\chi_{para}$  and  $\chi_{dia}$ . By quantifying the changes in iron and myelin

simultaneously, we may be better equipped to differentiate PD from HC and unveil a more comprehensive understanding of PD pathology. On the other hand, our study also yields interesting results regarding the trends of  $\chi_{para}$  and  $\chi_{dia}$  in the selected WM fiber bundles (Figure 14e,f). In particular, we observed complementary trends of  $\chi_{para}$  and  $\chi_{dia}$ , suggesting that myelin synthesis is accompanied by the iron accumulation in these WM fibers. This finding reinforces the view of the indispensable role of iron in myelination (Ortiz et al., 2004) and provides new insights into the longitudinal influence of iron deficiency on the functional development of the nervous system, such as the long-term effect of iron-deficiency anemia (IDA) on auditory and visual system (Algarin et al., 2003).

## 4.2 | Potential applications of sub-voxel QSM atlases

In this work, we constructed the longitudinal and age-specific atlases of QSM,  $\chi_{para}$  and  $\chi_{dia}$ . The longitudinal atlas provides high efficiency

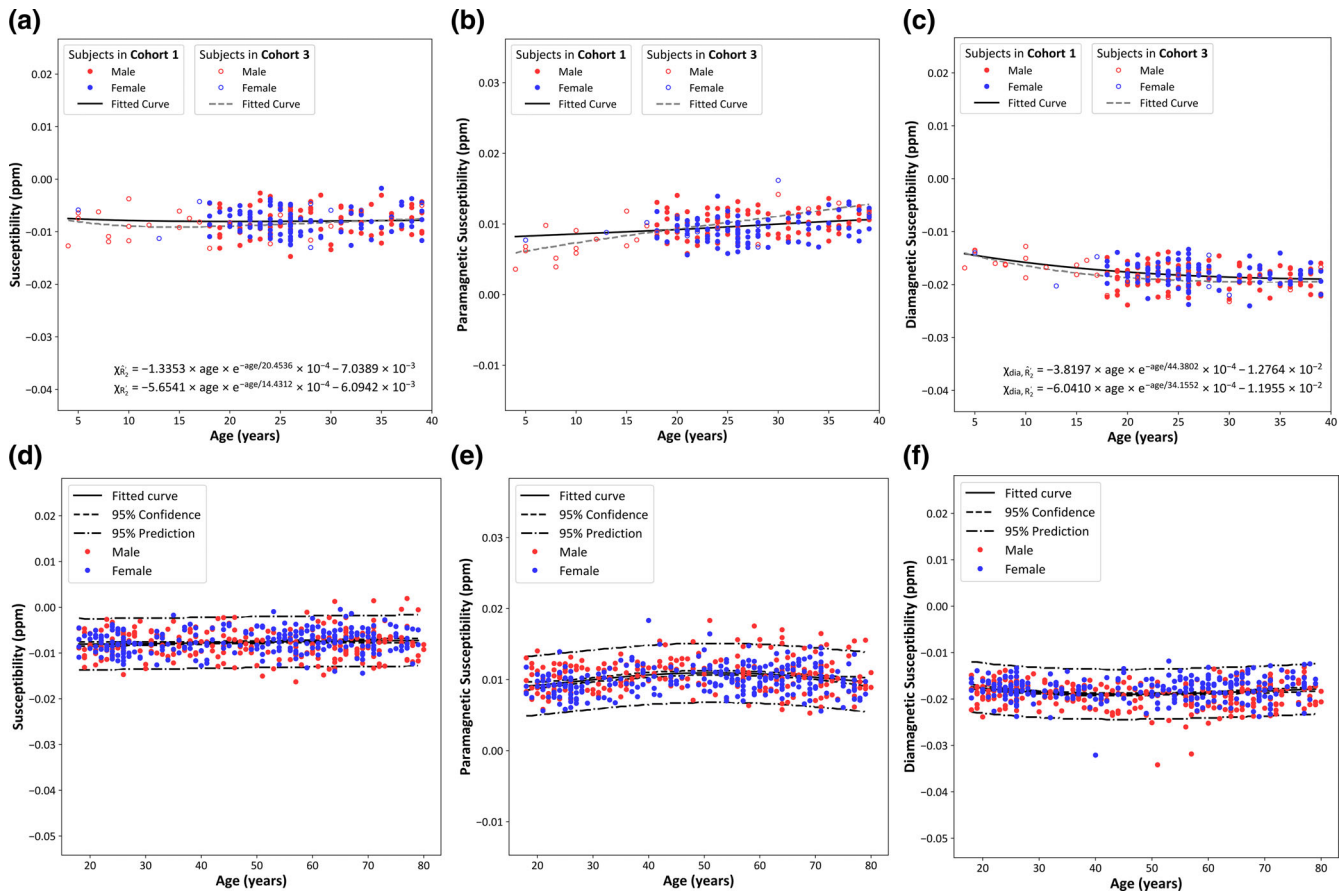


**FIGURE 14** The developmental trajectories of susceptibility with aging in Retrolen IC. (a–c) The comparison of QSM,  $\chi_{para}$  and  $\chi_{dia}$  trajectories in Cohort 1 (the solid curves and closed circles) and Cohort 3 (the dashed curves and open circles) from the age of 4 to 39. Red points: male, blue points: female. (d–f) The QSM,  $\chi_{para}$  and  $\chi_{dia}$  trajectory in Cohort 1 over the adult lifespan. The solid, dashed and dash-dot curves represent the fitted trajectories, 95% confidence and prediction intervals, respectively.

for projecting the individual susceptibility maps into the common space. The age-specific atlases reduce the bias introduced by age differences in the longitudinal atlas and assist in the regional analysis at each age interval. Moreover, the age-specific atlases of  $\chi_{para}$  and  $\chi_{dia}$  (Figure 6b,c) could provide a clear and comprehensive representation of the typical variation in iron and myelin during brain development, such as the iron accumulation with aging in the posterior part of Pu and the gradual myelination process in GP.

In addition, the constructed sub-voxel QSM atlases deliver improved magnetic susceptibility contrast compared to conventional QSM, enabling clearer boundary definition for small brain nuclei. For instance, Figure 6c exhibits the prominent WM fiber in the internal medullary lamina of the thalamus and the aging-associated myelination process in this area. In comparison, such differentiation is scarcely noticeable in the conventional QSM atlases (Figure 6a). As a result, these atlases potentially serve as an efficient segmentation tool for precise sub-region visualization and delineation. For instance, accurate segmentation can be achieved in structurally and functionally complex

brain regions, such as the thalamus and hippocampus, using the atlases of  $\chi_{para}$  and  $\chi_{dia}$ . This sub-region segmentation is beneficial not only for the target localization in neurosurgery, particularly in deep brain stimulation (DBS) planning, but also for exploring and diagnosing nervous system diseases.

### 4.3 | Limitations and future work

In this work, the susceptibility separation was performed using the first-order approximation of  $R_2'$  map, which might introduce systematic error to the result. This approximation relies on the assumption that the susceptibility-induced  $R_2^*$  and  $R_2'$  maps are approximately proportional under small concentrations of susceptibility sources (Bloembergen & Morgan, 1961; Yablonskiy & Haacke, 1994), which has been validated in the previous study (Dimov et al., 2022). In our study, a constant component representing the residual term in  $R_2$  was introduced to the first-order approximation model. The good spatial

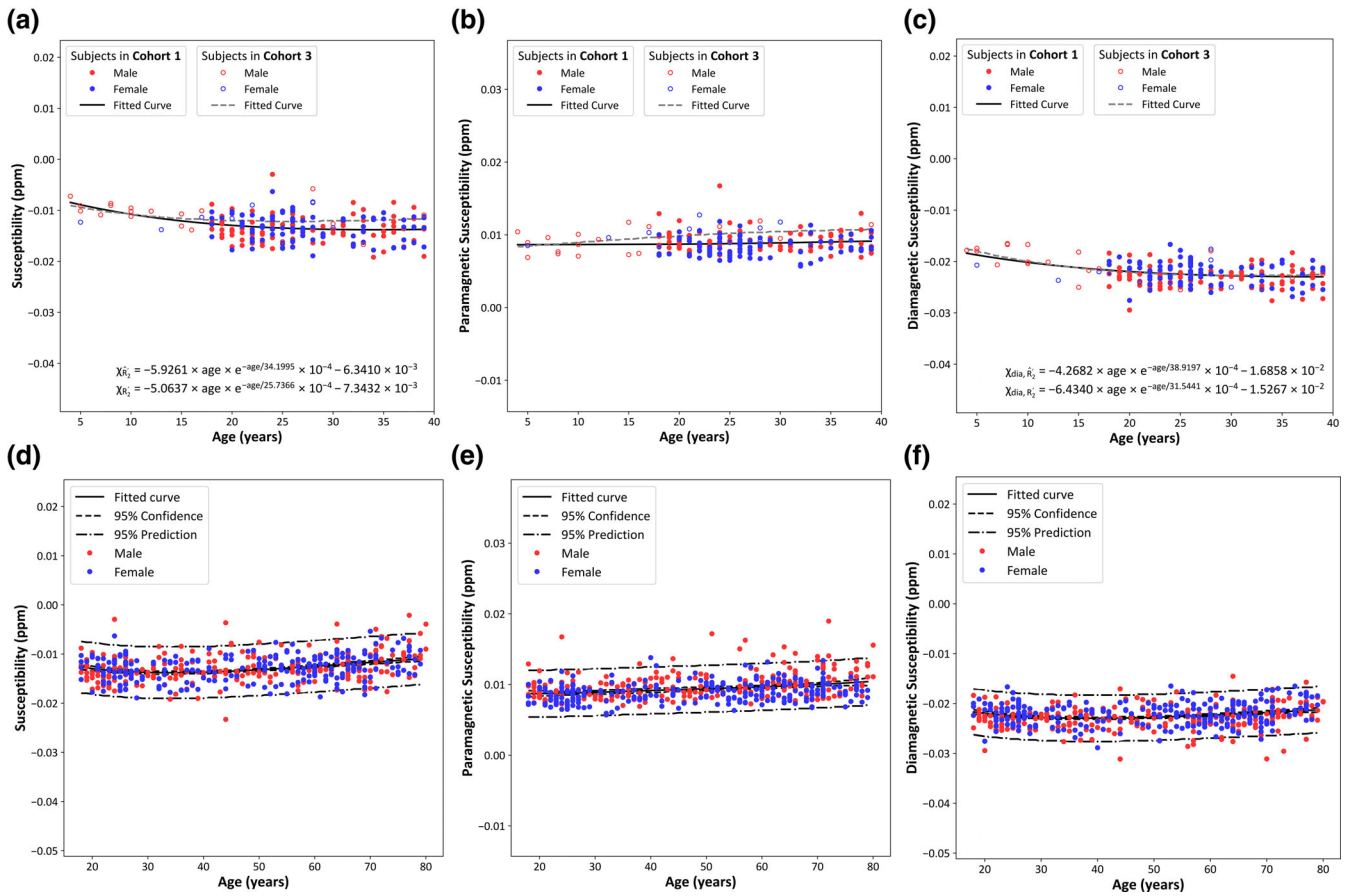


**FIGURE 15** The developmental trajectories of susceptibility with aging in SCC. (a–c) The comparison of QSM,  $\chi_{para}$  and  $\chi_{dia}$  trajectories in **Cohort 1** (the solid curves and closed circles) and **Cohort 3** (the dashed curves and open circles) from the age of 4 to 39. Red points: male, blue points: female. (d–f) The QSM,  $\chi_{para}$  and  $\chi_{dia}$  trajectory in **Cohort 1** over the adult lifespan. The solid, dashed and dash-dot curves represent the fitted trajectories, 95% confidence and prediction intervals, respectively.

agreement between the results of  $R_2'$ -based and  $\widehat{R_2}$ -based susceptibility separation supports its feasibility. Furthermore, the high consistency between the developmental trajectories derived from  $R_2'$ -based susceptibility separation (**Cohort 3**) and  $\widehat{R_2}$ -based susceptibility separation (**Cohort 1**) also indicates that this systematic error induced by the approximation of  $R_2'$  could be ignored under the large cohort condition.

The precise separation of susceptibility necessitates  $R_2$  mapping acquired using a multi-echo SE sequence, which is time-consuming and not feasible for data collection in large cohorts. Recently, the proposed multi-contrast imaging techniques have the potential to speed up data acquisition. For example, both MR multitasking (Cao et al., 2022) and BUDA-SAGE (Z. Zhang et al., 2022) are able to simultaneously obtain  $R_2^*$  and  $R_2$  mapping from a single MRI scan. However, these techniques still suffered from the inaccurate  $R_2^*$  value estimation and lengthy reconstruction time. Future research should concentrate on further reducing the reconstruction time and improving quantitative accuracy.

## 5 | CONCLUSION

Our study investigated the developmental trajectories of sub-voxel paramagnetic and diamagnetic susceptibility of brain tissues across the lifespan. The longitudinal and age-specific atlases of paramagnetic and diamagnetic susceptibility provide a standard coordinate space and efficient segmentation tool for sub-region delineation. Notably, this study, for the first time, uncovered the evolution of myelin in brain DGM and iron accumulation in WM in vivo. The findings indicate that the myelination process behaves at various rates among different nuclei in DGM. The complementary trajectories of paramagnetic and diamagnetic susceptibility highlight the essential role of iron deposition in myelin synthesis within WM. In summary, the longitudinal trajectory of sub-voxel QSM delivers valuable and comprehensive insights into the spatial and temporal patterns of iron deposition and myelination/demyelination concurrently during brain aging. This may expand our understanding of susceptibility alternation in various neurological diseases and help



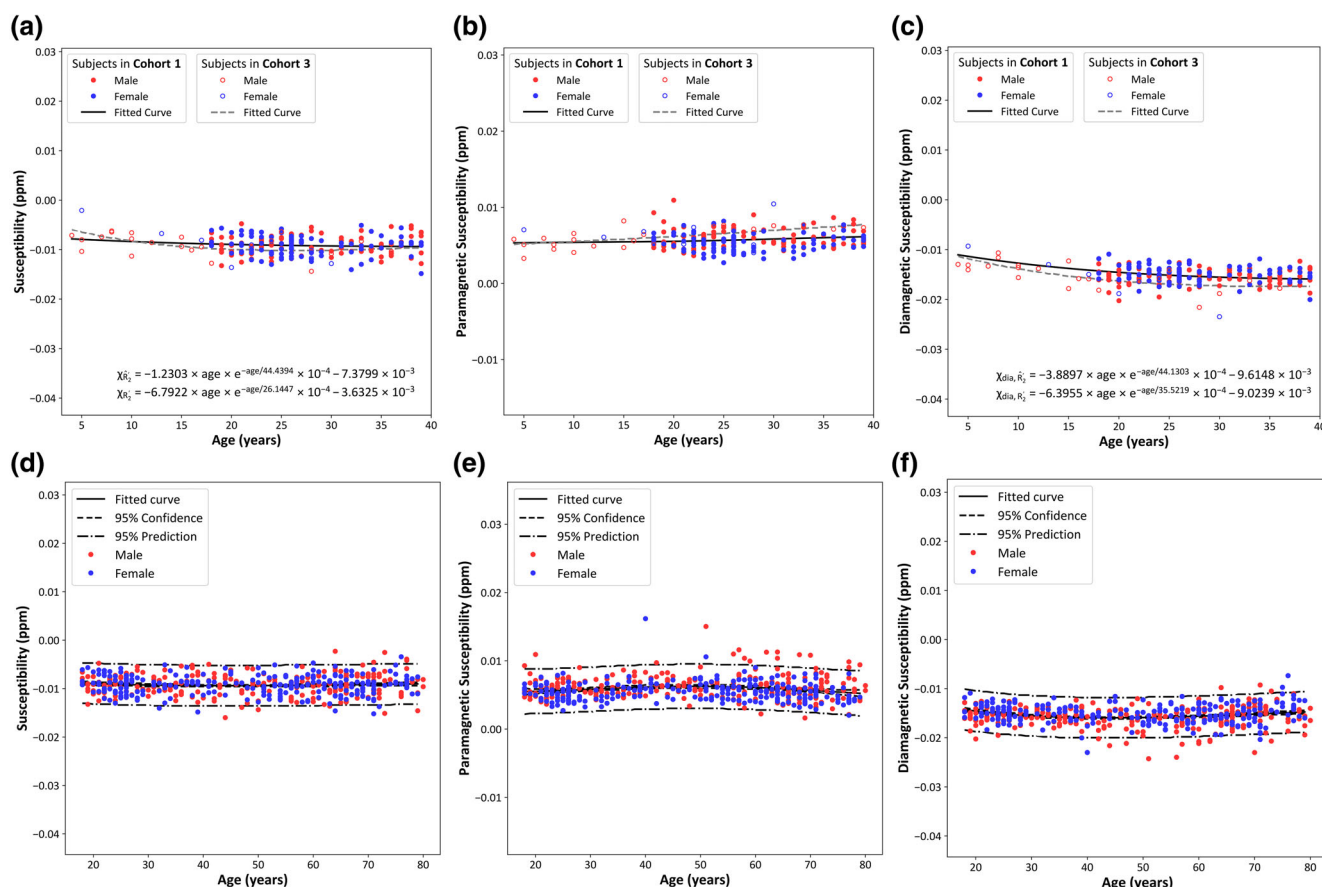


**FIGURE 16** The developmental trajectories of susceptibility with aging in Post CR. (a–c) The comparison of QSM,  $\chi_{para}$  and  $\chi_{dia}$  trajectories in **Cohort 1** (the solid curves and closed circles) and **Cohort 3** (the dashed curves and open circles) from the age of 4 to 39. Red points: male, blue points: female. (d–f) The QSM,  $\chi_{para}$  and  $\chi_{dia}$  trajectory in **Cohort 1** over the adult lifespan. The solid, dashed and dash-dot curves represent the fitted trajectories, 95% confidence and prediction intervals, respectively.

unveil the pathological processes of neurodevelopmental and neurodegenerative disorders.

## ACKNOWLEDGMENTS

This study is supported by the National Natural Science Foundation of China (61901256, 91949120, 62071299), the Fundamental Research Funds for the Central Universities, Young Leading Scientists Cultivation Plan supported by Shanghai Municipal Education Commission (ZXWH1082101), Shanghai Science and Technology Development Funds (21DZ1100300) and SJTU Trans-med Awards Research (STAR 20220103).

## CONFLICT OF INTEREST STATEMENT

The authors declare no conflict of interest.

## DATA AVAILABILITY STATEMENT

The constructed atlases for paramagnetic and diamagnetic susceptibility are publicly available at <https://github.com/AMRI-Lab/SubVoxel-QSM-Atlas>. The data that support the findings of this study are available from the corresponding author upon reasonable request.

## ORCID

Guoyan Lao  <https://orcid.org/0000-0002-2214-2419>

Xiaojun Xu  <https://orcid.org/0000-0002-0127-2812>

## REFERENCES

- Algarin, C., Peirano, P., Garrido, M., Pizarro, F., & Lozoff, B. (2003). Iron deficiency anemia in infancy: Long-lasting effects on auditory and visual system functioning. *Pediatric Research*, 53(2), 217–223. <https://doi.org/10.1203/01.PDR.0000047657.23156.55>
- Avants, B. B., Yushkevich, P., Pluta, J., Minkoff, D., Korczykowski, M., Detre, J., & Gee, J. C. (2010). The optimal template effect in hippocampus studies of diseased populations. *NeuroImage*, 49(3), 2457–2466. <https://doi.org/10.1016/j.neuroimage.2009.09.062>
- Bao, L., Xiong, C., Wei, W., Chen, Z., van Zijl, P. C. M., & Li, X. (2021). Diffusion-regularized susceptibility tensor imaging (DRSTI) of tissue microstructures in the human brain. *Medical Image Analysis*, 67, 101827. <https://doi.org/10.1016/j.media.2020.101827>
- Bartzokis, G., Lu, P. H., Tishler, T. A., Fong, S. M., Oluwadara, B., Finn, J. P., Huang, D., Bordelon, Y., Mintz, J., & Perlman, S. (2007). Myelin breakdown and iron changes in Huntington's disease: Pathogenesis and treatment implications. *Neurochemical Research*, 32(10), 1655–1664. <https://doi.org/10.1007/s11064-007-9352-7>

- Betts, M. J., Acosta-Cabrero, J., Cardenas-Blanco, A., Nestor, P. J., & Duzel, E. (2016). High-resolution characterisation of the aging brain using simultaneous quantitative susceptibility mapping (QSM) and R2\* measurements at 7T. *NeuroImage*, 138, 43–63. <https://doi.org/10.1016/j.neuroimage.2016.05.024>
- Biasioli, L., Lindsay, A. C., Chai, J. T., Choudhury, R. P., & Robson, M. D. (2013). In-vivo quantitative T2 mapping of carotid arteries in atherosclerotic patients: Segmentation and T2 measurement of plaque components. *Journal of Cardiovascular Magnetic Resonance: Official Journal of the Society for Cardiovascular Magnetic Resonance*, 15(1), 69. <https://doi.org/10.1186/1532-429X-15-69>
- Bloembergen, N., & Morgan, L. O. (1961). Proton relaxation times in paramagnetic solutions. Effects of electron spin relaxation. *The Journal of Chemical Physics*, 34(3), 842–850. <https://doi.org/10.1063/1.1731684>
- Cao, T., Ma, S., Wang, N., Gharabaghi, S., Xie, Y., Fan, Z., Hogg, E., Wu, C., Han, F., Tagliati, M., Haacke, E. M., Christodoulou, A. G., & Li, D. (2022). Three-dimensional simultaneous brain mapping of T1, T2, T2\* and magnetic susceptibility with MR multitasking. *Magnetic Resonance in Medicine*, 87(3), 1375–1389. <https://doi.org/10.1002/mrm.29059>
- Chen, J., Gong, N. J., Chaim, K. T., Otaduy, M. C. G., & Liu, C. (2021). Decompose quantitative susceptibility mapping (QSM) to sub-voxel diamagnetic and paramagnetic components based on gradient-echo MRI data. *NeuroImage*, 242, 118477. <https://doi.org/10.1016/j.neuroimage.2021.118477>
- Connor, J. R. (2004). Myelin breakdown in Alzheimer's disease: A commentary. *Neurobiology of Aging*, 25(1), 45–47. <https://doi.org/10.1016/j.neurobiolaging.2003.06.004>
- Dimov, A. V., Nguyen, T. D., Gillen, K. M., Marcille, M., Spincemaille, P., Pitt, D., Gauthier, S. A., & Wang, Y. (2022). Susceptibility source separation from gradient echo data using magnitude decay modeling. *Journal of Neuroimaging*, 32(5), 852–859. <https://doi.org/10.1111/jon.13014>
- German, K. R., & Juul, S. E. (2021). Iron and neurodevelopment in preterm infants: A narrative review. *Nutrients*, 13(11), 3737. <https://doi.org/10.3390/nu13113737>
- Haacke, E. M., Cheng, N. Y. C., House, M. J., Liu, Q., Neelavalli, J., Ogg, R. J., Khan, A., Ayaz, M., Kirsch, W., & Obenaus, A. (2005). Imaging iron stores in the brain using magnetic resonance imaging. *Magnetic Resonance Imaging*, 23(1), 1–25.
- Hallgren, B., & Sourander, P. (1958). The effect of age on the non-haemin iron in the human brain. *Journal of Neurochemistry*, 3(1), 41–51. <https://doi.org/10.1111/j.1471-4159.1958.tb12607.x>
- Hasan, K. M., Kamali, A., Iftikhar, A., Kramer, L. A., Papanicolaou, A. C., Fletcher, J. M., & Ewing-Cobbs, L. (2009). Diffusion tensor tractography quantification of the human corpus callosum fiber pathways across the lifespan. *Brain Research*, 1249, 91–100. <https://doi.org/10.1016/j.brainres.2008.10.026>
- He, C., Guan, X., Zhang, W., Li, J., Liu, C., Wei, H., Xu, X., & Zhang, Y. (2022). Quantitative susceptibility atlas construction in Montreal neurological institute space: Towards histological-consistent iron-rich deep brain nucleus subregion identification. *Brain Structure & Function*, 228, 1045–1067. <https://doi.org/10.1007/s00429-022-02547-1>
- Larsen, B., Bourque, J., Moore, T. M., Adebimpe, A., Calkins, M. E., Elliott, M. A., Gur, R. C., Gur, R. E., Moberg, P. J., Roalf, D. R., Ruparel, K., Turetsky, B. I., Vandekar, S. N., Wolf, D. H., Shinohara, R. T., & Satterthwaite, T. D. (2020). Longitudinal development of brain iron is linked to cognition in youth. *The Journal of Neuroscience*, 40(9), 1810–1818. <https://doi.org/10.1523/JNEUROSCI.2434-19.2020>
- Lebel, C., Gee, M., Camicioli, R., Wielers, M., Martin, W., & Beaulieu, C. (2012). Diffusion tensor imaging of white matter tract evolution over the lifespan. *NeuroImage*, 60(1), 340–352. <https://doi.org/10.1016/j.neuroimage.2011.11.094>
- Lee, H., Cho, H., Lee, M. J., Kim, T. H., Roh, J., & Lee, J. H. (2021). Differential effect of iron and myelin on susceptibility MRI in the substantia nigra. *Radiology*, 301(3), 682–691. <https://doi.org/10.1148/radiol.2021210116>
- Li, W., Avram, A. V., Wu, B., Xiao, X., & Liu, C. (2014). Integrated Laplacian-based phase unwrapping and background phase removal for quantitative susceptibility mapping. *NMR in Biomedicine*, 27(2), 219–227. <https://doi.org/10.1002/nbm.3056>
- Li, W., Wu, B., Batrachenko, A., Bancroft-Wu, V., Morey, R. A., Shashi, V., Langkammer, C., De Bellis, M. D., Ropele, S., Song, A. W., & Liu, C. (2014). Differential developmental trajectories of magnetic susceptibility in human brain gray and white matter over the lifespan. *Human Brain Mapping*, 35(6), 2698–2713. <https://doi.org/10.1002/hbm.22360>
- Li, W., Wu, B., & Liu, C. (2011). Quantitative susceptibility mapping of human brain reflects spatial variation in tissue composition. *NeuroImage*, 55(4), 1645–1656. <https://doi.org/10.1016/j.neuroimage.2010.11.088>
- Li, Z., Feng, R., Liu, Q., Feng, J., Lao, G., Zhang, M., Li, J., Zhang, Y., & Wei, H. (2023). APART-QSM: An improved sub-voxel quantitative susceptibility mapping for susceptibility source separation using an iterative data fitting method. *NeuroImage*, 274, 120148. <https://doi.org/10.1016/j.neuroimage.2023.120148>
- Liu, C., Wei, H., Gong, N. J., Cronin, M., Dibb, R., & Decker, K. (2015). Quantitative susceptibility mapping: Contrast mechanisms and clinical applications. *Tomography*, 1(1), 3–17. <https://doi.org/10.18383/j.tom.2015.00136>
- Massey, L. A., & Yousry, T. A. (2010). Anatomy of the substantia nigra and subthalamic nucleus on MR imaging. *Neuroimaging Clinics of North America*, 20(1), 7–27. <https://doi.org/10.1016/j.nic.2009.10.001>
- Mori, S., Wakana, S., Van Zijl, P. C., & Nagae-Poetscher, L. (2005). *MRI atlas of human white matter*. Elsevier.
- Naidich, T. P., Castillo, M., Cha, S., & Smirniotopoulos, J. G. (2012). *Imaging of the brain: Expert radiology series*. Elsevier Health Sciences.
- Ortiz, E., Pasquini, J. M., Thompson, K., Felt, B., Butkus, G., Beard, J., & Connor, J. R. (2004). Effect of manipulation of iron storage, transport, or availability on myelin composition and brain iron content in three different animal models. *Journal of Neuroscience Research*, 77(5), 681–689. <https://doi.org/10.1002/jnr.20207>
- Ramos, P., Santos, A., Pinto, N. R., Mendes, R., Magalhaes, T., & Almeida, A. (2014). Iron levels in the human brain: A post-mortem study of anatomical region differences and age-related changes. *Journal of Trace Elements in Medicine and Biology*, 28(1), 13–17. <https://doi.org/10.1016/j.jtemb.2013.08.001>
- Rolls, E. T., Huang, C.-C., Lin, C.-P., Feng, J., & Joliot, M. (2020). Automated anatomical labelling atlas 3. *NeuroImage*, 206, 116189. <https://doi.org/10.1016/j.neuroimage.2019.116189>
- Roncagliolo, M., Garrido, M., Walter, T., Peirano, P., & Lozoff, B. (1998). Evidence of altered central nervous system development in infants with iron deficiency anemia at 6 mo: Delayed maturation of auditory brainstem responses. *The American Journal of Clinical Nutrition*, 68(3), 683–690. <https://doi.org/10.1093/ajcn/68.3.683>
- Schaltenbrand, G., & Wahren, W. (1977). *Atlas for Stereotaxy of the human brain*. Thieme.
- Schofield, M. A., & Zhu, Y. (2002). Fast and robust phase unwrapping algorithm for electron holography. *Microscopy and Microanalysis*, 8(S02), 532–533. <https://doi.org/10.1017/s1431927602105228>
- Schweser, F., Deistung, A., Lehr, B. W., & Reichenbach, J. R. (2011). Quantitative imaging of intrinsic magnetic tissue properties using MRI signal phase: An approach to in vivo brain iron metabolism? *NeuroImage*, 54(4), 2789–2807. <https://doi.org/10.1016/j.neuroimage.2010.10.070>
- Shin, H.-G., Lee, J., Yun, Y. H., Yoo, S. H., Jang, J., Oh, S.-H., Nam, Y., Jung, S., Kim, S., Fukunaga, M., Kim, W., Choi, H. J., & Lee, J. (2021).  $\chi$ -Separation: Magnetic susceptibility source separation toward iron and myelin mapping in the brain. *NeuroImage*, 240, 118371. <https://doi.org/10.1016/j.neuroimage.2021.118371>
- Todorich, B. M., & Connor, J. R. (2004). Redox metals in Alzheimer's disease. *Annals of the New York Academy of Sciences*, 1012, 171–178. <https://doi.org/10.1196/annals.1306.014>

- Treit, S., Naji, N., Seres, P., Rickard, J., Stolz, E., Wilman, A. H., & Beaulieu, C. (2021).  $R_2^*$  and quantitative susceptibility mapping in deep gray matter of 498 healthy controls from 5 to 90 years. *Human Brain Mapping*, 42(14), 4597–4610. <https://doi.org/10.1002/hbm.25569>
- Virtanen, P., Gommers, R., Oliphant, T. E., Haberland, M., Reddy, T., Cournapeau, D., Burovski, E., Peterson, P., Weckesser, W., Bright, J., van der Walt, S. J., Brett, M., Wilson, J., Millman, K. J., Mayorov, N., Nelson, A. R. J., Jones, E., Kern, R., Larson, E., ... SciPy 1.0 Contributors. (2020). SciPy 1.0: Fundamental algorithms for scientific computing in python. *Nature Methods*, 17(3), 261–272. <https://doi.org/10.1038/s41592-019-0686-2>
- Ward, R. J., Zucca, F. A., Duyn, J. H., Crichton, R. R., & Zecca, L. (2014). The role of iron in brain ageing and neurodegenerative disorders. *The Lancet. Neurology*, 13(10), 1045–1060. [https://doi.org/10.1016/S1474-4422\(14\)70117-6](https://doi.org/10.1016/S1474-4422(14)70117-6)
- Wei, H., Dibb, R., Zhou, Y., Sun, Y., Xu, J., Wang, N., & Liu, C. (2015). Streaking artifact reduction for quantitative susceptibility mapping of sources with large dynamic range. *NMR in Biomedicine*, 28(10), 1294–1303. <https://doi.org/10.1002/nbm.3383>
- Wu, B., Li, W., Guidon, A., & Liu, C. (2012). Whole brain susceptibility mapping using compressed sensing. *Magnetic Resonance in Medicine*, 67(1), 137–147. <https://doi.org/10.1002/mrm.23000>
- Yablonskiy, D. A., & Haacke, E. M. (1994). Theory of NMR signal behavior in magnetically inhomogeneous tissues: The static dephasing regime. *Magnetic Resonance in Medicine*, 32(6), 749–763.
- Zhang, Y., Wei, H., Cronin, M. J., He, N., Yan, F., & Liu, C. (2018). Longitudinal atlas for normative human brain development and aging over the lifespan using quantitative susceptibility mapping. *NeuroImage*, 171, 176–189. <https://doi.org/10.1016/j.neuroimage.2018.01.008>
- Zhang, Z., Cho, J., Wang, L., Liao, C., Shin, H. G., Cao, X., Lee, J., Xu, J., Zhang, T., Ye, H., Setsompop, K., Liu, H., & Bilgic, B. (2022). Blip up-down acquisition for spin- and gradient-echo imaging (BUDA-SAGE) with self-supervised denoising enables efficient T2, T2\*, Para- and diamagnetic susceptibility mapping. *Magnetic Resonance in Medicine*, 88(2), 633–650. <https://doi.org/10.1002/mrm.29219>

## SUPPORTING INFORMATION

Additional supporting information can be found online in the Supporting Information section at the end of this article.

**How to cite this article:** Lao, G., Liu, Q., Li, Z., Guan, X., Xu, X., Zhang, Y., & Wei, H. (2023). Sub-voxel quantitative susceptibility mapping for assessing whole-brain magnetic susceptibility from ages 4 to 80. *Human Brain Mapping*, 44(17), 5953–5971. <https://doi.org/10.1002/hbm.26487>